

Analytical and numerical study of uncorrelated disorder on a honeycomb lattice

Kean Loon Lee,¹ Benoît Grémaud,^{2,1,3} Christian Miniatura,^{4,1,3} and Dominique Delande²

¹Centre for Quantum Technologies, National University of Singapore, 3 Science Drive 2, Singapore 117543, Singapore

²Laboratoire Kastler-Brossel, UPMC-Paris 6, ENS, CNRS; 4 Place Jussieu, F-75005 Paris, France

³Department of Physics, National University of Singapore, 2 Science Drive 3, Singapore 117542, Singapore

⁴INLN, Université de Nice-Sophia Antipolis, CNRS; 1361 route des Lucioles, 06560 Valbonne, France

We consider a tight-binding model on the regular honeycomb lattice with uncorrelated on-site disorder. We use two independent methods (recursive Green's function and self-consistent Born approximation) to extract the scattering mean free path, the scattering mean free time, the density of states and the localization length as a function of the disorder strength. The two methods give excellent quantitative agreement for these single-particle properties. Furthermore, a finite-size scaling analysis reveals that all localization lengths for different lattice sizes and different energies (including the energy at the Dirac points) collapse onto a single curve, in agreement with the one-parameter scaling theory of localization. The predictions of the self-consistent theory of localization however fail to quantitatively reproduce these numerically-extracted localization lengths.

I. INTRODUCTION

Anderson localization (AL) of waves [1] in disordered media is a ubiquitous phenomenon which has been observed both for classical and quantum waves, e.g. light [2, 3], acoustics [4, 5], water waves [6], ultracold atoms [7, 8], polaritons [9] and quantum Hall system [10]. The scaling theory of localization [11] predicts that a three-dimensional (3D) system exhibits a metal-insulator transition while 1D and 2D systems always display localization at any finite disorder strength. Approximate analytical expressions for the localization length in terms of the transport mean free path can be derived within the framework of the self-consistent theory of localization [12, 13]. Dimension two is in fact the critical dimension for AL and symmetry considerations can play an important role. Indeed, while localization is expected to take place for spinless time-reversal invariant systems (albeit with an exponentially large localization length), perturbative renormalization group studies on non-linear σ -models suggest that a metal-insulator transition may occur in 2D if chirality is present [14, 15]. Such a disordered system with different chiral classes could be realized with the honeycomb lattice. The successful isolation of graphene flakes in 2004 [16], and the discovery that graphene samples exhibit a finite electronic conductivity at half-filling although the density of states (DoS) vanishes [17, 18], has thus spurred interest in studying electronic transport in graphene in the presence of disorder, see [19] and references therein.

However, even though graphene is a readily-available physical realization of a honeycomb lattice, its properties are invariably affected by the combined effects of interaction, disorder and phonons. The controlled study of disorder alone in graphene sheets is thus difficult, notwithstanding the fact that engineering disorder with given statistical properties seems out of reach. In that respect, ultracold atoms loaded on a graphene-like optical lattice [20–22] offer an alternative route and have already proven their key impact in weak and strong localization

studies [7, 23–27]. Furthermore, key transport quantities, like the scattering and transport mean free paths or the localization length, have already been analyzed for speckle optical potentials in the Born approximation in Ref. [13] while engineering disorder with different correlation properties is possible.

The aim of this paper is to study transport in a disordered honeycomb lattice. We first stick to the simpler case of the tight-binding model for the regular honeycomb lattice in the presence of uncorrelated on-site disorder characterized by a symmetric box distribution. The more interesting (but more complicated) case of correlated on-site disorder will be the scope of a forthcoming publication. The novelty of our work lies in the generalization of two known methods, the recursive Green's function method and the self-consistent Born approximation, (i) to extract single-particle properties, such as the scattering mean free time τ , the scattering mean free path ℓ , the density of state (DoS) ν , and the localization length ξ , and (ii) to relate them to experimentally-controlled parameters, such as the tunneling amplitude J and the disorder strength W . The numerical data obtained from these two methods show remarkable agreement and give an accurate estimation of these single-particle properties. Our results further confirm the one-parameter scaling hypothesis [11] for localization but also reveal a quantitative disparity with the predictions of the self-consistent theory of localization [12, 13]. This disparity is yet to be understood.

Currently, there are three pieces of numerical works that are technically relevant to ours. Using a transfer matrix technique, Schreiber and Ottomeier [28] have shown that the localization lengths for various lattices (square, honeycomb and triangular) at the energy band centre $E = 0$ – thus including the Dirac point of the honeycomb lattice – and for various disorder strengths obey the same scaling laws. Using the same method, Xiong and Xiong concluded that all states are localized but found that the scaling behavior at the charge neutrality point is different from the one at different energies [29]. On the other hand, Lherbier et al. considered the time dynamics of a ran-

dom phase wave packet using a real space order- N Kubo method [30]. They subsequently extracted the diffusion constant, and hence the scattering mean free path (which coincides with the transport mean free path as scattering by our δ -correlated potential is isotropic), from the time evolution of the spatial spread of the wave packet. This extracted scattering mean free path was then used to deduce the semi-classical conductivity through Einstein-Kubo relation [31] and the localization length through the self-consistent theory of localization, a procedure that our numerical data question.

The paper is organized as follows. Sec. II gives the essential ingredients of our model and the eigenstructure of the disorder-free honeycomb lattice in the tight-binding regime. In Sec. III, we introduce the self-energy and detail the Born and self-consistent Born approximations (SCBA). We further derive analytical expressions for the self-energy at some particular energies in the weak-disorder limit. In Sec. IV, we introduce the recursive Green's function (RGF) method which is designed to compute exact matrix elements of the Green's function for large system sizes, with the caveat that actual computations can take months on a computer cluster. A faster but more restricted variant is the recursive transfer matrix method. Together with a finite-size analysis, these methods allow us to extract the localization length of the disordered honeycomb lattice at any given energy. In Sec. V, we perform a finite-size analysis of the localization lengths. We show that they can be simultaneously scaled for all energies, including the charge neutrality point. Furthermore, our results indicate that this universal curve is valid for all lattice types, all energies within the energy band and possibly for all types of uncorrelated disorders, which is not surprising from the viewpoint of the one-parameter scaling hypothesis. In addition to the localization length, we also extract the scattering mean free path and the DoS from the recursive Green's function method evaluated at complex energies. The extracted quantities show remarkable agreement with our results from the self-consistent Born approximation. The comparison of the numerically computed localization length to the prediction of the self-consistent theory of localization shows a fair qualitative agreement, but marked quantitative differences. We finally conclude in Sec. VI. Additional details are given in the Appendices.

II. MODEL

We consider here a tight-binding Hamilton operator acting on a regular honeycomb lattice with on-site disorder

$$H = H_0 + V = -J \sum_{\langle i,j \rangle} (|i\rangle\langle j| + |j\rangle\langle i|) + \sum_i \varepsilon_i |i\rangle\langle i|, \quad (1)$$

where $|i\rangle$ refers to a Wannier state localized on site i and $\langle i,j \rangle$ denotes a sum over nearest neighbors. The hopping parameter J is usually positive and it fixes the energy

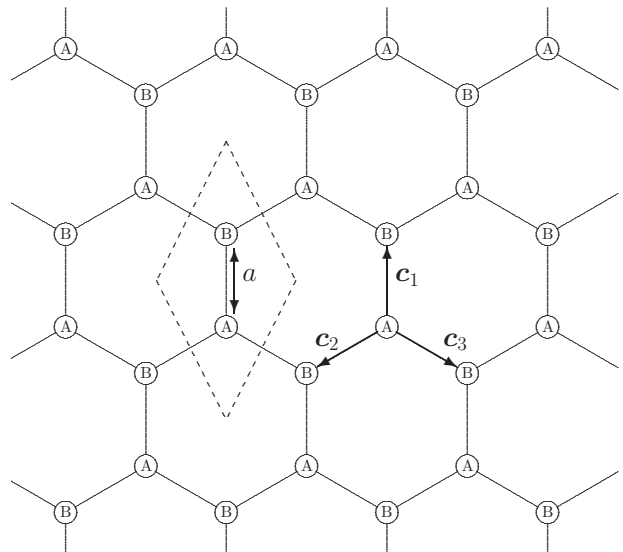


FIG. 1. A honeycomb lattice with lattice constant a and its diamond-shaped two-point basis cell (dashed line). The vectors \mathbf{c}_l ($l = 1, 2, 3$) connect an A-site to its three B-site nearest-neighbors.

scale. Throughout the paper, we assume the diagonal elements ε_i to be independent random variables characterized by the same symmetric box probability distribution

$$P(\varepsilon_i) = \begin{cases} \frac{1}{W} & \text{for } |\varepsilon_i| \leq \frac{W}{2}, \\ 0 & \text{otherwise.} \end{cases} \quad (2)$$

where W is the disorder strength. The disorder has thus zero mean average $\overline{\varepsilon_i} = 0$ and its two-point correlator is then $C_{ij} = \overline{\varepsilon_i \varepsilon_j} = \frac{W^2}{12} \delta_{ij}$, where the bar denotes averaging over disorder configurations. The disorder being spatially δ -correlated, scattering is isotropic; the scattering and transport mean free paths are consequently equal.

We now briefly review the eigenstructure of the disorder-free Hamiltonian H_0 . We refer to Ref. [20] for more details. The regular honeycomb lattice being a triangular Bravais lattice with a two-site basis cell, it can be pictured as two shifted triangular sublattices denoted by A and B, see Fig. 1. As a consequence, the coordination number of the honeycomb lattice is three. We denote by \mathbf{c}_l ($l = 1, 2, 3$) the link vectors connecting a site $i \in A$ to its three nearest-neighbors $j_l \in B$ ($|\mathbf{c}_l| = a$, a being the lattice constant). We next define the structure factor of the honeycomb lattice for nearest-neighbor hopping as

$$f(\mathbf{k}) = |f(\mathbf{k})| e^{i\varphi(\mathbf{k})} = \sum_{l=1}^3 e^{i\mathbf{k} \cdot \mathbf{c}_l}. \quad (3)$$

For the honeycomb lattice depicted in Fig. 1, where \mathbf{c}_1 points along the y -axis, we have

$$|f(\mathbf{k})|^2 = 1 + 4 \cos^2 \left(\frac{\sqrt{3}k_x a}{2} \right) + 4 \cos \left(\frac{\sqrt{3}k_x a}{2} \right) \cos \left(\frac{3k_y a}{2} \right). \quad (4)$$

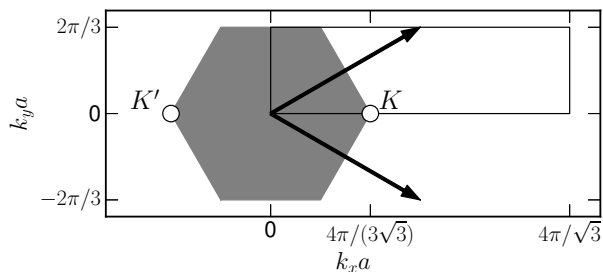


FIG. 2. The first Brillouin zone \mathcal{B} (in grey) of the honeycomb lattice shown in Fig. 1 and the associated reciprocal lattice vectors (arrows). The two empty circles mark the Dirac points, around which the energy dispersion is linear. By using convenient reciprocal lattice translations, the first Brillouin zone can be mapped onto the shown rectangle which is then used as the integration space in all integrals in the paper.

As shown in Ref. [20], the eigenstructure of H_0 is defined by

$$H_0 = \sum_{\mathbf{k} \in \mathcal{B}, s=\pm} \varepsilon_{\mathbf{k}s} |\mathbf{k}s\rangle \langle \mathbf{k}s|, \quad (5)$$

$$\varepsilon_{\mathbf{k}s} = s \varepsilon_{\mathbf{k}} = s J |f(\mathbf{k})|, \quad (6)$$

$$|\mathbf{k}s\rangle = \frac{1}{\sqrt{2N_c}} \left[\sum_{i \in A} e^{i\mathbf{k} \cdot \mathbf{r}_i} |i\rangle - s e^{-i\varphi(\mathbf{k})} \sum_{j \in B} e^{i\mathbf{k} \cdot \mathbf{r}_j} |j\rangle \right] \quad (7)$$

where \mathcal{B} is the first Brillouin zone of the honeycomb lattice (see Fig. 2), s is the band index ($s = +1$ for the upper, or conduction, band; $s = -1$ for the lower, or valence, band) and N_c is the number of Bravais cells of the lattice.

The full spectrum spans the energy interval $[-3J, 3J]$ and band crossing can only occur at zero energy since $\varepsilon_+(\mathbf{k}) = \varepsilon_-(\mathbf{k})$ implies that $f(\mathbf{k}) = 0$. This happens at the Dirac points \mathbf{K} and $\mathbf{K}' = -\mathbf{K}$ where

$$\mathbf{K} = \left(\frac{4\pi}{3\sqrt{3}a}, 0 \right) \quad (8)$$

for the honeycomb lattice in Fig. 1. In the solid-state community, the energy at the Dirac points is usually referred to as the charge neutrality (energy) point because the number of energy states above and below this point are equal. As a consequence, when the gate voltage is fixed at $\varepsilon_{\pm}(\mathbf{K}) = 0$ in a graphene sample, the graphene sheet is charge neutral since the particle and hole states are balanced.

In the rest of the paper, we will be mainly interested in the different localization properties of our model for energies E lying near the band edges, $E \approx \pm 3J$, and near the band centre, $E \approx 0$. In the first case, \mathbf{k} lies near the centre of the Brillouin zone ($ka \ll 1$, where $k = |\mathbf{k}|$), while in the second case \mathbf{k} lies near the Dirac points ($qa \ll 1$, where $\mathbf{q} = \mathbf{k} - \mathbf{K}$, and similarly around \mathbf{K}').

Near the band edges $E = \pm 3J$, the dispersion relation

is quadratic, thus representing free massive particles

$$\varepsilon_{\mathbf{k}s} \approx 3Js \left(1 - \frac{a^2 k^2}{4} \right) \quad ka \ll 1, \quad (9)$$

the effective mass $m_s = -s2\hbar^2/(3Ja^2)$ being negative for the upper band and positive for the lower band.

Near the charge neutrality point $E = 0$, the dispersion relation is linear, thus representing the celebrated “relativistic” massless Dirac particles propagating with a velocity c playing the role of an effective speed of light,

$$\varepsilon_{\mathbf{k}s} \approx s \frac{3J}{2} a q = s \hbar c q \quad (qa \ll 1), \quad (10)$$

$$c = \frac{3aJ}{2\hbar}. \quad (11)$$

III. SELF-ENERGY

An initial Bloch state $|\mathbf{k}s\rangle$ propagating in the lattice will suffer scattering by the disorder fluctuations and thus will be depleted, decaying exponentially over time with a time constant which is the scattering mean free time $\tau_{\mathbf{k}s}$. This coherent propagation and decay are described by the disorder-averaged Green’s function \overline{G} which obey the Dyson’s equation

$$\overline{G}(z) = G_0(z) + G_0(z) \Sigma(z) \overline{G}(z), \quad (12)$$

z being a point in the complex energy plane. Within our model, the disorder-free Green’s function is given by

$$G_0(z) = \frac{1}{z - H_0} = \sum_{\mathbf{k}s} \frac{|\mathbf{k}s\rangle \langle \mathbf{k}s|}{z - \varepsilon_{\mathbf{k}s}}. \quad (13)$$

The Dyson equation features the self-energy Σ which is a central quantity given by a perturbative sum of irreducible diagrams [32]. As the disorder average restores the lattice translation symmetries and characteristics, one has

$$\langle \mathbf{k}'s' | \overline{G}(z) | \mathbf{k}s \rangle = \overline{G}_{\mathbf{k}s}(z) \delta_{\mathbf{k}\mathbf{k}'} \delta_{ss'}, \quad (14)$$

$$\langle \mathbf{k}'s' | \Sigma(z) | \mathbf{k}s \rangle = \Sigma_{\mathbf{k}s}(z) \delta_{\mathbf{k}\mathbf{k}'} \delta_{ss'}, \quad (15)$$

where the dependence of $\Sigma_{\mathbf{k}s}(z)$ on \mathbf{k} is usually smooth. Due to particle-hole symmetry, the spectrum of H_0 is symmetric with respect to $E = 0$. Since the on-site energies are themselves independent symmetrically-distributed random variables, it is easy to show that $\langle \mathbf{k}s | \overline{G}(z) | \mathbf{k}s \rangle^* = -\langle \mathbf{k}, -s | \overline{G}(-z^*) | \mathbf{k}, -s \rangle$, where the star stands for complex conjugation. In turn, the self-energy satisfies ¹

$$\Sigma_{\mathbf{k},s}(z) = \Sigma_{\mathbf{k},-s}^*(-z^*). \quad (16)$$

¹ These identities no longer hold for a speckle potential since it breaks the $V \rightarrow -V$ symmetry.

Furthermore, because of time-reversal invariance, the self-energy is the same at $\pm\mathbf{k}$. This means that it is sufficient to study the negative energy sector and forward propagation ($k_x \geq 0$). The scattering mean free time, defined through

$$\frac{\hbar}{2\tau_{\mathbf{k}s}(E)} = -\text{Im}\Sigma_{\mathbf{k}s}(E), \quad (17)$$

is independent of the band index.

A. Born approximation

An analytical expression for $\Sigma_{\mathbf{k}s}(z)$ is generally not available and one has to resort to approximations to find the self-energy. For weak disorder, the simplest approximation is the Born approximation which consists in discarding all terms of the full diagrammatic perturbative expansion in Fig. 3 except the first one. Its lattice matrix elements are

$$\langle i|\Sigma_{\text{Born}}(z)|j\rangle = C_{ij} \langle i|G_0(z)|j\rangle = \frac{W^2}{12} I(z) \delta_{ij} \quad (18)$$

with

$$I(z) = \langle i|G_0(z)|i\rangle = \int_{\mathcal{B}} \frac{d\mathbf{k}}{\Omega} \frac{z}{z^2 - J^2|f(\mathbf{k})|^2}, \quad (19)$$

where $\Omega = 8\pi^2/(3\sqrt{3}a^2)$ is the area of the first Brillouin zone. For uncorrelated on-site disorder, the self-energy at the Born approximation is a scalar:

$$\Sigma_{\mathbf{k}s}(z) \approx \Sigma_{\text{Born}}(z) = \frac{W^2}{12} I(z). \quad (20)$$

The average Green's function then reads

$$\overline{G}_{\text{Born}}(z) = \frac{1}{z - H_0 - \Sigma_{\text{Born}}(z)} = G_0(z - \Sigma_{\text{Born}}(z)). \quad (21)$$

The expression of $I(z)$ in terms of elliptic integrals [33, 34] is given in Appendix A.

B. Self-consistent Born approximation (SCBA)

This approximation scheme builds on the Born approximation by replacing G_0 by \overline{G} in Eq. (18). It is more powerful as it amounts to sum the infinite subclass of “rainbow” diagrams given in Fig. 3. It gives the following self-consistent equation:

$$\Sigma_{\text{SCBA}}(z) = \frac{W^2}{12} \langle i|\overline{G}(z)|i\rangle = \frac{W^2}{12} I(z - \Sigma_{\text{SCBA}}(z)), \quad (22)$$

which is easy to solve numerically.

In the following we will use the parametrization $\Sigma_{\text{SCBA}}(z) = \gamma J e^{-i\theta}$ with γ positive. For the scattering time to be positive, we must have $\text{Im}\Sigma_{\mathbf{k}s} < 0$, which

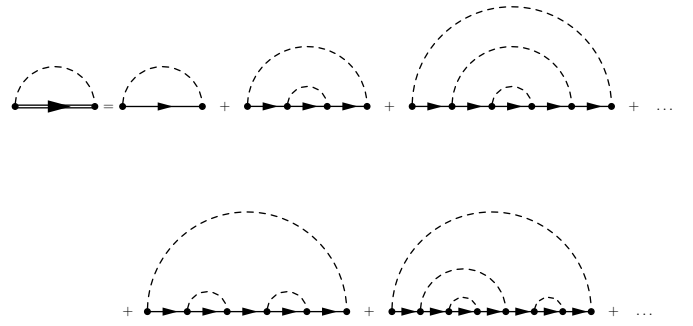


FIG. 3. The “rainbow” subclass of diagrams retained to compute the self-energy in the self-consistent Born approximation. The double line with arrow denotes an averaged Green’s function \overline{G} while a single line with arrow denotes a disorder-free lattice Green’s function G_0 . Two vertices (solid dots) connected by a dashed line represent a 2-point correlator $C_{ij} = \overline{\varepsilon_i \varepsilon_j}$. The Born approximation consists in computing the self-energy with the first “rainbow” diagram only. For uncorrelated disorder, the connected vertices correspond thus to the same site. In this case the self-energy is a scalar operator depending only on the energy and the disorder strength.

enforces $0 \leq \theta \leq \pi$. Eq. (16) then translate into

$$\gamma(-E, W) = \gamma(E, W) \quad (23)$$

$$\theta(-E, W) = \pi - \theta(E, W). \quad (24)$$

This implies $\theta(0, W) = \pi/2$ for any disorder strength W . Figs. 4 and 5 show the E -dependence of θ and γ in the SCBA for some particular disorder strengths W , while Figs. 6 and 7 show the W -dependence of θ and γ in the SCBA at some particular energies E . In the following subsection, we investigate SCBA analytically in the weak disorder regime.

C. Weak disorder limit

In the weak disorder regime $W \ll J$, one expects $\gamma \ll 1$. Several analytical results can then be derived in this limit. Some details are exposed in Appendix B.

1. Charge neutrality point

At the charge neutrality point, we have $z = E = 0$ and the function I in (22) is thus evaluated at the dimensionless complex number $Z = -\Sigma_{\text{SCBA}}(0, W)/J$. Furthermore, because of Eq. (16), $\theta(0, W) = \pi/2$, and $\Sigma_{\text{SCBA}}(0, W) = -i\gamma(0, W)J$ is purely imaginary. Equations (22) and (A3) have two solutions. One is the trivial solution $\gamma(0, W) = 0$ while the nontrivial solution solves

$$\int_{\mathcal{B}} \frac{d\mathbf{k}}{\Omega} \frac{1}{|f(\mathbf{k})|^2 + \gamma^2(0, W)} = \frac{12J^2}{W^2}. \quad (25)$$

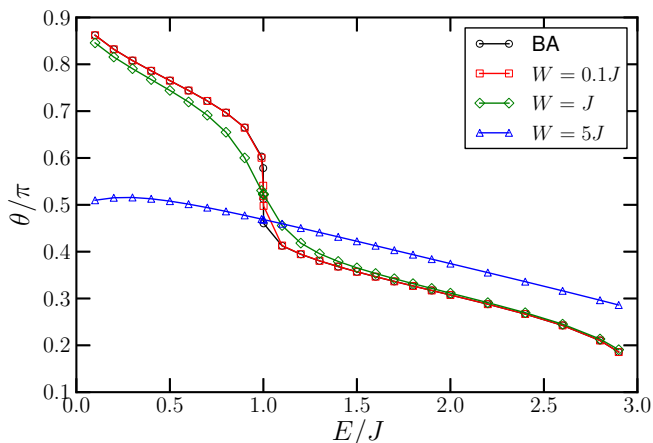


FIG. 4. (Color online) Using the parametrization $\Sigma(z) = \gamma J e^{-i\theta}$ ($\gamma \geq 0$, $0 \leq \theta \leq \pi$), the figure shows the angle θ as a function of the energy E in the Born approximation (black open circles) and in the SCBA for various disorder strengths. In the Born approximation, θ is independent of W . At $W = 0.1J$, SCBA and the Born approximation are essentially identical.

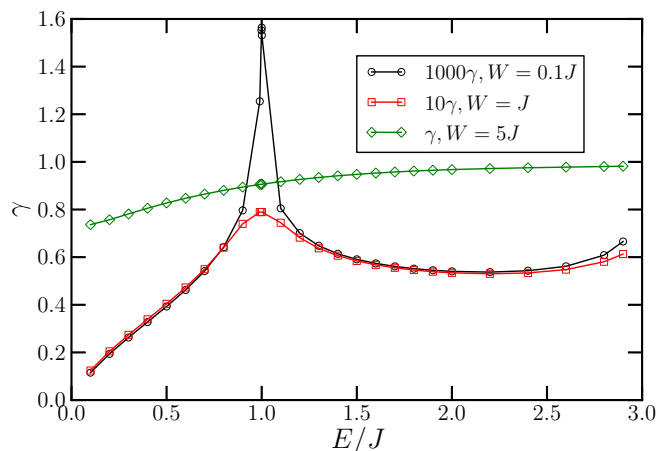


FIG. 5. (Color online) Using the parametrization $\Sigma(z) = \gamma J e^{-i\theta}$ ($\gamma \geq 0$, $0 \leq \theta \leq \pi$), the figure shows the amplitude γ as a function of the energy E in the SCBA for various disorder strengths. As $W \rightarrow 0$, the peak at $E = J$ develops into the van Hove singularity.

An expansion of the elliptic integrals appearing in the first line of Eq. (A3) for $|Z| \ll 1$ leads to

$$\gamma(0, W) \approx 3 \exp\left(-\frac{6\pi\sqrt{3}J^2}{W^2}\right). \quad (26)$$

Shon *et al.* found essentially the same type of result $\gamma J = \varepsilon_c \exp(-A_1/W^2)$, see Eq. (3.21) in [35]. The difference between their parameter values and ours arises from their introduction of the cut-off energy ε_c . In our treatment, we use the exact dispersion relation, beyond the linear approximation around the Dirac points, making

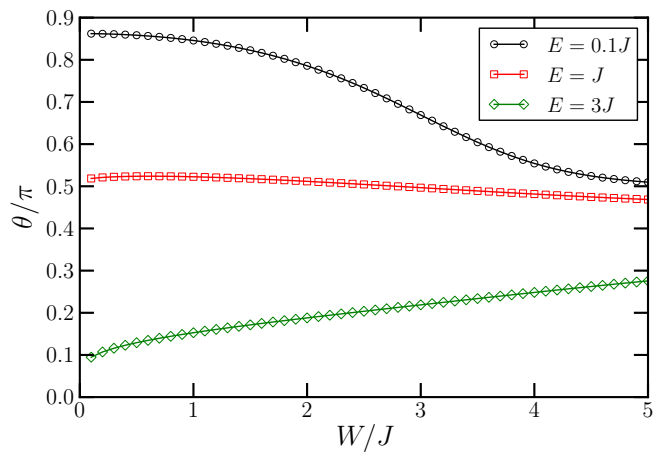


FIG. 6. (Color online) Using the parametrization $\Sigma(z) = \gamma J e^{-i\theta}$ ($\gamma \geq 0$, $0 \leq \theta \leq \pi$), the figure shows the angle θ as a function of the disorder strength W in the SCBA near the charge neutrality point, at the van Hove singularity and at the band edge.

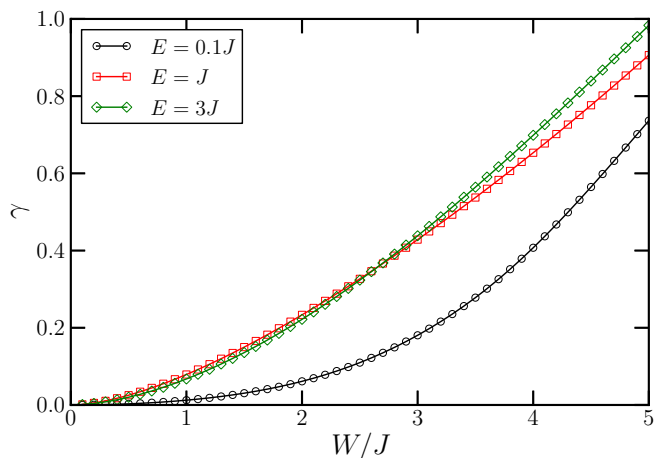


FIG. 7. (Color online) Using the parametrization $\Sigma(z) = \gamma J e^{-i\theta}$ ($\gamma \geq 0$, $0 \leq \theta \leq \pi$), the figure shows the amplitude γ as a function of the disorder strength W in the SCBA near the charge neutrality point, at the van Hove singularity and at the band edge.

the introduction of an artificial cut-off unnecessary.

2. Van Hove singularities

At the van Hove singularities, the disorder-free DoS diverges. For our honeycomb tight-binding model, this occurs at $z = E = \pm J$ [20] and the function I in (22) is now evaluated at the dimensionless complex number $Z_+ = 1 - \Sigma_{\text{SCBA}}(J, W)/J$. A small-parameter expansion

of equations (22) and (A3) around $Z = 1$ now leads to

$$\gamma(J, W) \approx \frac{W^2}{16\pi J} \left(\ln\left(\frac{64\pi J^2}{W^2}\right) + \ln\ln\left(\frac{64\pi J^2}{W^2}\right) \right), \quad (27)$$

$$\theta(J, W) \approx \frac{\pi}{2} \left(1 + \frac{1}{3 \left(\ln\left(\frac{64\pi J^2}{W^2}\right) - \ln\ln\left(\frac{64\pi J^2}{W^2}\right) \right)} \right). \quad (28)$$

One sees that, at lowest order, the self-energy at the van Hove singularities is purely imaginary too, $\theta \approx \pi/2$.

3. Band edges

At the disorder-free band edges, $z = E = \pm 3J$. By the same token, we evaluate the function I in (22) at the dimensionless complex number $Z_+ = 3 - \Sigma_{\text{SCBA}}(3J, W)/J$. A small-parameter expansion around $Z = 3$ now leads to

$$\begin{aligned} \Sigma_{\text{SCBA}}(3J, W) \approx & \frac{\sqrt{3}W^2}{48\pi J} \left(\ln\left(\frac{192\sqrt{3}\pi J^2}{W^2}\right) - i\pi \right. \\ & \left. - \ln\left(\ln\left(\frac{192\sqrt{3}\pi J^2}{W^2}\right) - i\pi\right) \right). \end{aligned} \quad (29)$$

Anticipating results displayed and discussed in Paragraph VC, within the SCBA scheme, the DoS vanishes outside a finite energy band, with a square-root behavior near the band edge. This SCBA band edge is approximately given by the solution of the equation $E - \text{Re}\Sigma_{\text{SCBA}}(E) = 3J$ and does not coincide with the exact band edge $3J + W/2$ found for the box disorder. Note also that the Lifshitz tail between $3J$ and $3J + W/2$ is completely missed by the SCBA scheme.

IV. RECURSIVE GREEN'S FUNCTION METHOD

The RGF method is based upon the division of the system in smaller sections for which the Green's functions

can be calculated more easily [36]. These sections are then “glued together” one after one and Dyson's equation [37] is repeatedly used to derive the full Green's function in terms of the Green's functions of the smaller sections. To study localization, we will use a generalized version [38, 39] of the RGF method. This generalized version enables us to extract *any* lattice matrix element of the Green's function conveniently and with high numerical stability.

Applying the RGF scheme to our case amounts to consider a finite quasi-1D lattice strip and to divide it into N vertical slices, the two open ends being along the horizontal direction, see Fig. 8. Denoting by H_{N-1} the nearest-neighbor tight-binding Hamilton operator for a strip with $(N-1)$ slices, the Hamilton operator H_N obtained by gluing an additional slice N can be split into three terms,

$$H_N = H_{N-1} + H_N^{\text{slice}} + H_{N-1, N}^{\text{hop}} + H_{N, N-1}^{\text{hop}}, \quad (30)$$

where $H_{N-1, N}^{\text{hop}}$ is the nearest-neighbor hop operator connecting sites within slice $(N-1)$ to sites within slice N (and vice-versa for $H_{N, N-1}^{\text{hop}}$). Since no external gauge fields are present in our model, we safely consider the hop operators to be real from now on. H_N^{slice} is the nearest-neighbor tight-binding Hamilton operator for the isolated slice N before it is stacked to the others. It thus includes the on-site disorder diagonal term V in Eq. (1).

Using Dyson's equation, the submatrix $G_{l, n}^{(N)}$ of the full retarded Green's function $G^{(N)} = (E + i0^+ - H_N)^{-1}$ coupling slice l to slice n at energy E can be obtained through the following recursion relations,

$$G_{l, n}^{(N)} = G_{l, n}^{(N-1)} + G_{l, N-1}^{(N-1)} H_{N-1, N}^{\text{hop}} G_{N, n}^{(N)}, \quad (31a)$$

$$G_{l, N}^{(N)} = G_{l, N-1}^{(N-1)} H_{N-1, N}^{\text{hop}} G_{N, N}^{(N)}, \quad (31b)$$

$$G_{N, n}^{(N)} = G_{N, N}^{(N)} H_{N, N-1}^{\text{hop}} G_{N-1, n}^{(N-1)}, \quad (31c)$$

$$G_{N, N}^{(N)} = \left(E + i0^+ - H_N^{\text{slice}} - H_{N, N-1}^{\text{hop}} G_{N-1, N-1}^{(N-1)} H_{N-1, N}^{\text{hop}} \right)^{-1} \quad (31d)$$

with $1 \leq l \leq n \leq (N-1)$, see Appendix C for a short derivation.

In the following subsections, we explain how we chose to slice the honeycomb lattice for the zigzag and arm-

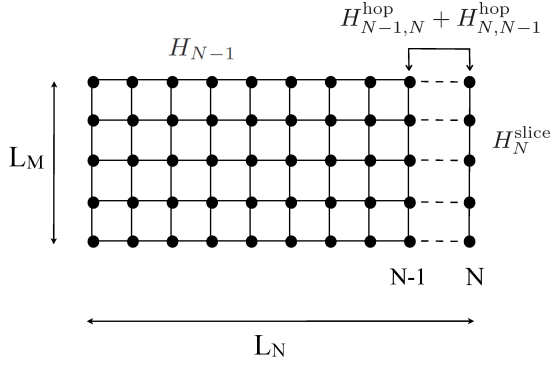


FIG. 8. Schematic illustration of the RGF method with a strip of square lattice of length L_N and width L_M . The system under consideration is constructed by repeated stacking of vertical slices of length L_M . The Green's function at each step of the stacking process is calculated recursively using Dyson's equation. Knowing the Green's function $G^{(N-1)} = (E + i0^+ - H_{N-1})^{-1}$ for the system with $(N-1)$ slices, the hop operator $H_N^{\text{hop}} = H_{N-1,N}^{\text{hop}} + H_{N,N-1}^{\text{hop}}$ coupling slices $(N-1)$ and N , and the Hamilton operator H_N^{slice} of the isolated slice N , one can exactly compute the Green's function $G^{(N)}$ for the whole system of N slices, see Eqs. (31).

chair geometries. Once the stacking is properly defined, each lattice site $i \equiv (n, m)$ will then be labelled by two integers. The first one $1 \leq n \leq N$ corresponds to the slice it belongs to from left to right, N being the total number of such slices. The second one $1 \leq m \leq M$ corresponds to its position along the slice from bottom to top, M being the total number of sites per slice. For both geometries we have checked that the matrix elements of the Green's function obtained through the recursive algorithm agree well with those computed by direct inversion of the operator $(E + i0^+ - H_N)$.

A. Zigzag configuration

We first consider the zigzag (ZZ) configuration depicted in Fig. 9, where L vertical zigzag chains of the honeycomb lattice are stacked along the horizontal direction. In the following we will be essentially interested in the case of periodic boundary conditions in the vertical direction and open boundary conditions in the horizontal one. This imposes the number of sites in each zigzag chain to be an even integer $2M$. For each zigzag chain, one can define A-type (resp. B-type) vertical slices containing only A-sites (resp. B-sites). Each of these vertical slices contain M sites and there are $N = 2L$ such slices, A-type slices alternating with B-type slices. Lattice sites are thus parametrized by (n, m) with $1 \leq n \leq N = 2L$ and $1 \leq m \leq M$, see Fig. 9. The width and length of this honeycomb ZZ strip are $L_M = \sqrt{3}Ma$ and $L_N \approx 3Na/4$ ($N \gg 1$).

With this slicing choice, the Hamiltonian H_n^{slice} associated to the isolated slice n is simply a $M \times M$ diagonal

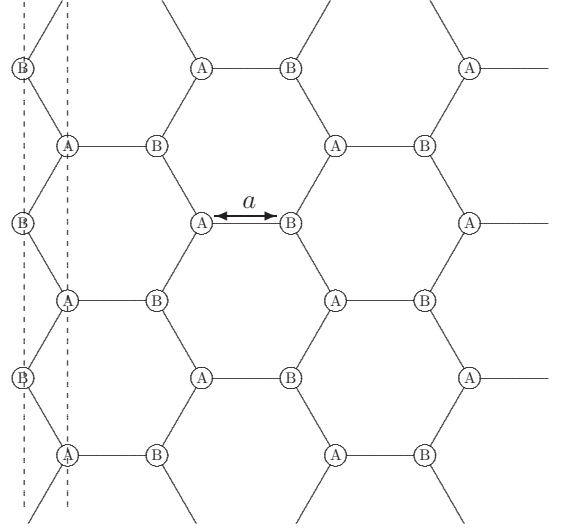


FIG. 9. In the honeycomb zigzag configuration with periodic boundary conditions along the vertical direction, L zigzag vertical chains, each containing $2M$ sites, are stacked along the horizontal direction ($L = 4$ and $M = 3$ in the figure). Each zigzag chain defines two vertical slices (dashed vertical lines). These slices are labeled from left to right by the integer $1 \leq n \leq N = 2L$. Each slice contains M sites labeled from bottom to top by the integer $1 \leq m \leq M$. The slice gender alternates between A-type and B-type. Each site in the lattice is uniquely parametrized by the couple of integers (n, m) .

matrix with entries given by the M on-site disorder elements $\{\varepsilon_{n,m}\}$. Furthermore, one can easily see that

$$\begin{aligned} H_{n,n+1}^{\text{hop}} &= -J \mathbb{1} && \text{if } n \equiv 0 \pmod{4} \\ H_{n,n+1}^{\text{hop}} &= -J \mathbf{D} && \text{if } n \equiv 1 \pmod{4} \\ H_{n,n+1}^{\text{hop}} &= -J \mathbb{1} && \text{if } n \equiv 2 \pmod{4} \\ H_{n,n+1}^{\text{hop}} &= -J \mathbf{D}^T && \text{if } n \equiv 3 \pmod{4} \\ H_{n+1,n}^{\text{hop}} &= (H_{n,n+1}^{\text{hop}})^T \end{aligned} \quad (32)$$

where the T-superscript means matrix transposition and \mathbf{D} is the $M \times M$ matrix given by

$$\mathbf{D} = \begin{pmatrix} 1 & 0 & 0 & \cdots & 0 & p \\ 1 & 1 & 0 & \cdots & 0 & 0 \\ 0 & 1 & 1 & \cdots & 0 & 0 \\ \vdots & \vdots & \vdots & \ddots & \vdots & \vdots \\ 0 & 0 & 0 & \cdots & 1 & 1 \end{pmatrix}. \quad (33)$$

When periodic boundary conditions in the vertical direction are used (which is our case), $p = 1$. For open boundary conditions in the vertical direction, one would have $p = 0$.

An astute reader may have noticed that the determinant of \mathbf{D} vanishes for M even and periodic boundary conditions. In this case the transfer matrix method [36] cannot be implemented as it would require the inversion

of \mathbf{D} or \mathbf{D}^T . To avoid this pitfall, one can nevertheless always choose M odd. Note however that the RGF scheme is perfectly immune to this breakdown and its implementation does not suffer any flaw as we have duly checked.

B. Armchair configuration

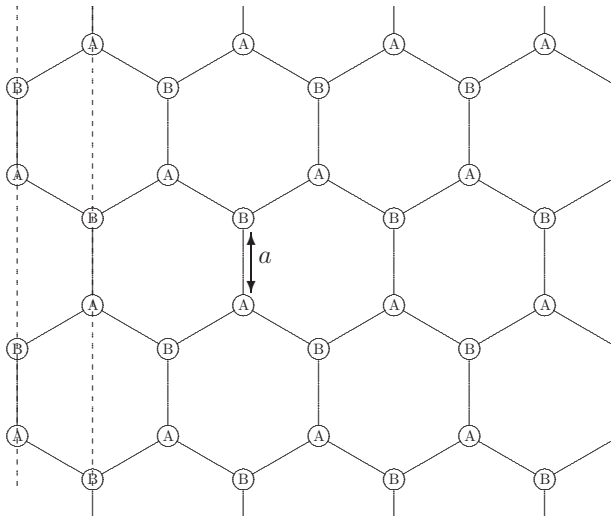


FIG. 10. In the armchair configuration (AC), M horizontal zigzag chains, each containing N sites, are stacked vertically ($M = 4$ and $N = 8$ in the figure). There are thus N vertical slices labeled from left to right by the integer $1 \leq n \leq N$ (dashed lines). Each vertical slice contains M sites labeled from bottom to top by the integer $1 \leq m \leq M$. If periodic boundary conditions are imposed along the vertical direction, M must be even. The site gender within a slice alternates between A-type and B-type. Each site in the lattice is uniquely parametrized by the couple of integers (n, m) .

We now turn to the honeycomb armchair configuration where M horizontal zigzag chains, each containing N sites, are stacked along the vertical direction, see Fig. 10. When periodic boundary conditions are imposed along the vertical direction, M must be even. The left vertical boundary of the lattice is now reminiscent of the shape of an armchair. Using the same recipe, we slice the lattice with vertical lines. There are now N such vertical slices, each containing M sites. The width and length of this honeycomb AC strip are $L_M = 3Ma/2$ and $L_N \approx \sqrt{3}Na/2$ ($N \gg 1$).

In the armchair configuration, it is easy to see that the $M \times M$ hop matrices satisfy $H_{n,n+1}^{\text{hop}} = H_{n+1,n}^{\text{hop}} = -J\mathbb{1}$, while $H_n^{\text{slice}} = -J\mathbf{X}_n + \varepsilon_n$ where ε_n is a $M \times M$ diagonal matrix with entries equal to the M on-site disorder $\{\varepsilon_{n,m}\}$ in slice n . \mathbf{X}_n is a $M \times M$ sparse matrix that couples each site to its nearest neighbors within slice

n , namely

$$\mathbf{X}_n = \begin{cases} \begin{pmatrix} 0 & 1 & 0 & 0 & \cdots & 0 & 0 \\ 1 & 0 & 0 & 0 & \cdots & 0 & 0 \\ 0 & 0 & 0 & 1 & \cdots & 0 & 0 \\ 0 & 0 & 1 & 0 & \cdots & 0 & 0 \\ \vdots & \vdots & \vdots & \vdots & \ddots & \vdots & \vdots \\ 0 & 0 & 0 & 0 & \cdots & 0 & 1 \\ 0 & 0 & 0 & 0 & \cdots & 1 & 0 \end{pmatrix} & \text{if } n \text{ is odd,} \\ \begin{pmatrix} 0 & 0 & 0 & 0 & 0 & \cdots & 0 & 0 & p \\ 0 & 0 & 1 & 0 & 0 & \cdots & 0 & 0 & 0 \\ 0 & 1 & 0 & 0 & 0 & \cdots & 0 & 0 & 0 \\ 0 & 0 & 0 & 0 & 1 & \cdots & 0 & 0 & 0 \\ 0 & 0 & 0 & 1 & 0 & \cdots & 0 & 0 & 0 \\ \vdots & \vdots & \vdots & \vdots & \vdots & \ddots & \vdots & \vdots & \vdots \\ 0 & 0 & 0 & 0 & 0 & \cdots & 0 & 1 & 0 \\ 0 & 0 & 0 & 0 & 0 & \cdots & 1 & 0 & 0 \\ p & 0 & 0 & 0 & 0 & \cdots & 0 & 0 & 0 \end{pmatrix} & \text{if } n \text{ is even,} \end{cases} \quad (34)$$

where $p = 1$ for periodic boundary conditions along the vertical direction (and M even) and $p = 0$ for open ones.

V. NUMERICAL RESULTS

A. Localization length ξ

Localized wave functions are expected to decrease exponentially at large distances. We thus compute the localization length along the horizontal direction as ²

$$\frac{2}{\lambda_M} = - \lim_{N \rightarrow \infty} \frac{1}{L_N} \overline{\ln \text{Tr} \left(J^2 G_{1,N}^{(N)} [G_{1,N}^{(N)}]^\dagger \right)}, \quad (35)$$

where the bar indicates the average over disorder configurations. Note that it corresponds to the log-averaged transmission in quasi-1D systems which has the nice property of being additive and self-averaging when new slices are added [40].

This finite-size localization length λ_M depends on the energy E and the disorder strength W , but also on the lattice configuration (ZZ or AC) and width L_M . In all our simulations, we have used a sufficiently large number of randomly-generated disorder configurations for each set of parameters (E , W , M and lattice configuration) such that the estimated relative error in computing $1/\lambda_M$ is less than 0.2%. Furthermore $1/\lambda_M$ is always computed with lengths L_N greater than $5\lambda_M$. This means that larger number of samples are required as λ_M increases. To avoid numerical underflow, a rescaling of $G_{1,N}^{(N)}$ is done through Eq. (31b) every 10 multiplications

² Some authors define the localization length λ_M through $\overline{\ln |\psi|}$ (as we do here) or through $\overline{\ln |\psi|^2}$. There is a factor of 2 between these two possible definitions.

approximately. RGF equations require one matrix inversion per slice. To speed up the computation for the AC lattice we switched to the recursive transfer matrix method [36] where a true matrix inversion is carried out only after the transfer matrix equation is applied for 10 slices.

Based on ideas of the renormalization group [36] and the scaling theory of localization [11], it was conjectured that all data points in a λ_M/L_M versus ξ/L_M plot should collapse onto the same universal curve,

$$\frac{\lambda_M}{L_M} = F\left(\frac{\xi}{L_M}\right) \quad (36)$$

where the infinite-lattice localization length ξ depends only on energy E and disorder strength W . Our results in Fig. 11 fully supports this conjecture for sufficiently large L_M .

When $L_M \gg \xi$, the system becomes insensitive to the vertical boundary conditions and one expects $\lambda_M \approx \xi$. The scaling function should thus satisfy $F(x) \approx x$ for small x . We chose the honeycomb AC configuration at $E = 3J$ and $W = 10J$ as the reference data set for this limiting behavior, therefore fixing $\xi = (2.46 \pm 0.01)a$ in this case, see black data at the bottom left corner in Fig. 11. At finite system width, we nevertheless expect the computed localization length λ_M to be slightly shorter than the true infinite-lattice localization length ξ . This behavior is accounted for by a Taylor expansion of the scaling function $F(x) = x - \alpha x^2 + O(x^3)$. From our data we infer $\alpha = (1.11 \pm 0.01)$.

Starting from the situation at small x , the full scaling function $F(x)$ is then built by finding, for each of our data sets, the corresponding ξ allowing to patch them on a single smooth curve. This procedure has been done with our AC data sets obtained in the range $E \in [0.1J, 3J]$ and $W \in [1.2J, 10J]$. We have also checked that AC data sets obtained for E slightly larger than $3J$ and various W , as well as ZZ data sets obtained at different energies ($E = 0.4J, J, 2.9J$) and $W = 1.6J$, all collapse onto this very same curve too. In particular, we numerically confirm that at $E = 0.4J$, $E = 2.9J$, and $W = 1.6J$, we get the same ξ for the ZZ and AC configurations. This might be understood as a consequence of the isotropic dispersion relation in the two energy ranges, see Eqs. (9) and (11). On the other hand, at $E = J$, the extracted ξ are slightly different for the two honeycomb configurations.

For the AC configuration, an important finding is that data sets obtained at the charge neutrality point ($E = 0$) for $W \geq 2.5J$ can all be scaled by $F(x)$. Fig. 12 shows the collapsed data for $W = 2.5J, 4J$ and $6J$ ($\xi = 500a, 70.9a$ and $16.9a$ respectively). Performing similar calculations for different lattice models (honeycomb, square and triangular), Schreiber and Ottomeier also found that their data obtained at $E = 0$ and $W \geq 4J$ could be collapsed onto a single universal curve [28]. Since our data at $W = 4J$ and $6J$ with $M = 46$ agree with theirs at $M = 40$ (after proper unit conversion), we infer that we indeed found the same universal curve.

While it is difficult to numerically confirm that data at $E = 0$ and $W < 2.5J$ can be scaled by $F(x)$ (see analysis below for the reason of this difficulty), there is no apparent reason why they should not. Therefore, our results, combined with those in Ref. [28], imply that all curves λ_M/L_M as a function of $1/L_M$ can be collapsed onto the same universal curve by an appropriate one-parameter scaling, independently of the lattice type and disorder strength, at least for uncorrelated box-distributed on-site disorder and energies within (and slightly outside of) the energy band of the clean system. This is in marked contrast with the findings of Ref. [29], which claim a different scaling behavior at $E = 0$ (see below for a possible explanation of this apparent contradiction).

For the clean system near $E = 0$, the energy shell slices the band structure near the Dirac points, defining two circles of allowed wavevectors centred on \mathbf{K} and $-\mathbf{K}$. The initial state $|\mathbf{k}s\rangle$ belongs to one of these circles, say the one around \mathbf{K} . Introducing the deviation wavevector $\mathbf{q} = \mathbf{k} - \mathbf{K}$, the circles have radius $|\mathbf{q}|$. In the presence of disorder, the two circles are broadened in the energy shell and form rings of allowed wavevectors with mean radius $|\mathbf{q}|$. Since disorder is uncorrelated in space, the two rings are coupled by scattering. However, the scattering processes being elastic, starting from the initial state \mathbf{q} , only these two rings around the Dirac points will be populated in the course of time. Loosely speaking, if scattering does change the direction of \mathbf{q} , it cannot change its modulus. Around $E = 0$, the dynamics is thus characterized by small wavevectors, i.e. by long distances in real space. This is why we expect finite-size effects to be larger around $E = 0$. This can be seen in Fig. 13 where the dependence of λ_M on L_M shows a damped oscillatory behavior when L_M/a is not large enough. As explained below, the very existence of oscillations can be traced back to the opening of new scattering channels when L_M increases whereas the damping can be traced back to disorder broadening.

Consider the finite-size AC configuration. For periodic boundary conditions, the allowed values for the wavevector \mathbf{k} along Ox and Oy are quantized according to $k_x = n_x \Delta k_N$ and $k_y = n_y \Delta k_M$ with $\Delta k_N = 2\pi/L_N$, $\Delta k_M = 2\pi/L_M$, $n_x \in \{0, \dots, N\}$ and $n_y \in \{0, \dots, M\}$. In the vicinity of $E = 0$, the curve at constant E will enclose a small circular area around the Dirac point K in the Brillouin zone containing few such discrete points. When the system size, notably L_M , is increased, more points enter this area, which means that more channels open for propagation. The period of the oscillations observed in Fig. 13 thus corresponds to the change in L_M allowing one new channel to open, i.e. $\Delta L_M = 2\pi/q$, where q is the radius of the circle at energy E . Using Eq. (11), we estimate the period of the oscillations to be roughly of the order of $\Delta L_M = 3\pi a J/|E|$. However, each quantized \mathbf{k} -mode corresponding to energy E is broadened by disorder, typically by ℓ^{-1} . As a consequence modes cannot be distinguished from each other when $\Delta k_M \ell \approx 1$. Near the Dirac point, one has $\ell = c\tau$

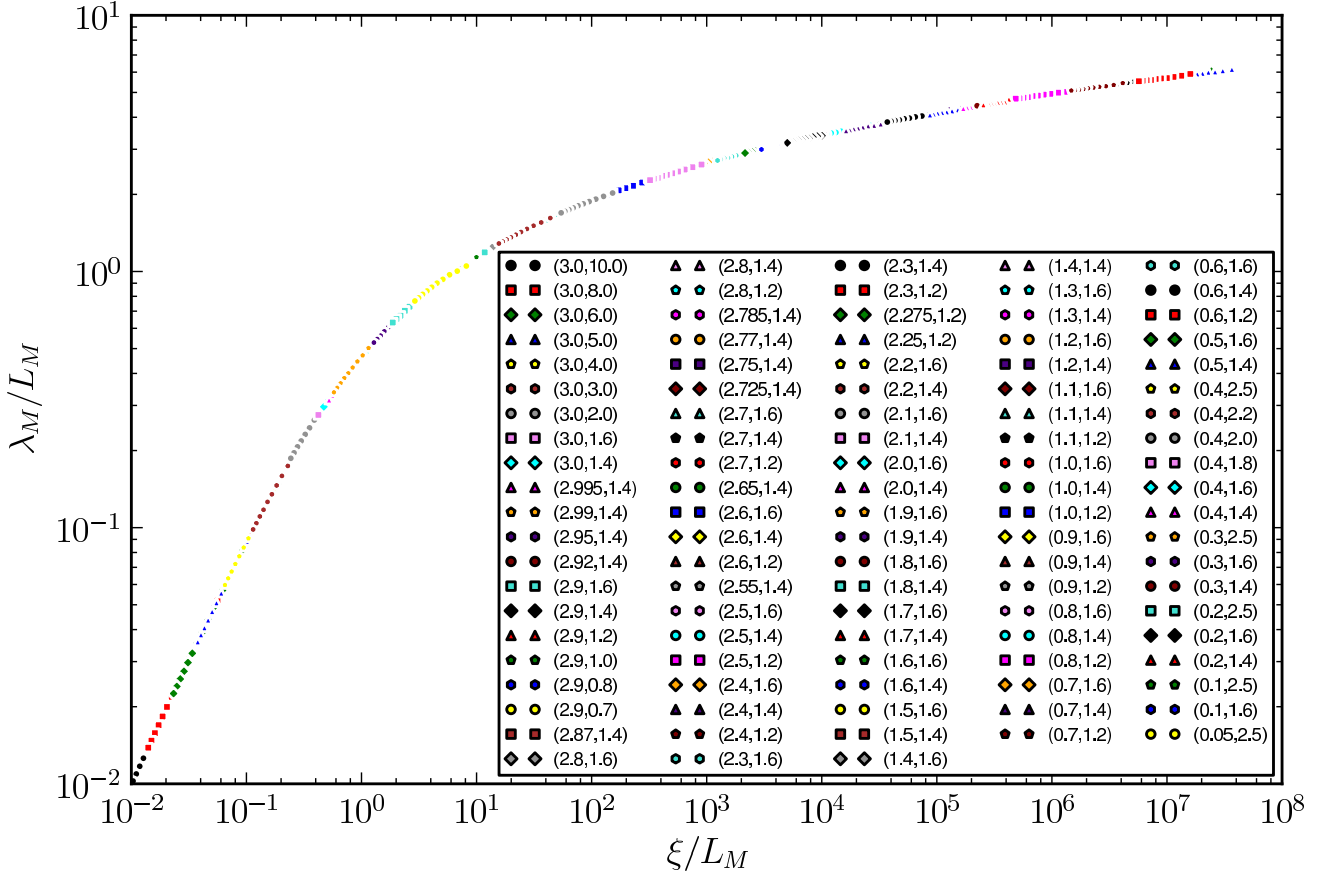


FIG. 11. (Color online) Single-parameter scaling law for the AC honeycomb lattice with uncorrelated on-site disorder. We numerically compute the finite-size localization length λ_M at various energy $0.1J \leq E \leq 3J$ and disorder strength $1.2J \leq W \leq 10J$. The fact that all data sets can be collapsed onto a single log-log curve where ξ is the infinite-lattice localization length confirms the scaling theory of localization [11]. Each disjoint color represents a parameter pair (E, W) as shown in the inset.

and we find that the oscillations due to the opening of new channels are washed out as soon as

$$\frac{a}{L_M} \lesssim -\frac{2\text{Im}\Sigma(E, W)}{3\pi J}. \quad (37)$$

Using SCBA at $W = 1.6J$, this simple estimate gives $a/L_M \approx 4 \times 10^{-3}$ at $E = 0.1J$ and $a/L_M \approx 7.4 \times 10^{-3}$ at $E = 0.2J$, in perfect agreement with the data collected in Fig. 13.

To obtain a reliable estimate of ξ , it is necessary to go beyond the oscillatory region. This is numerically challenging at $E = 0$ for weak disorder, see (26). For example, the SCBA estimate at $W = 1.6J$ now gives $a/L_M \approx 2 \times 10^{-6}$, way out of the capabilities of the RGF scheme. We believe this is the reason why a different scaling at $E = 0$ was claimed in [29]: the sample sizes used by the Authors were probably not large enough to reach the scaling region. As seen in Fig. 13, it is easy to miss the oscillations at $E = 0$ for small W . The curve there is clearly different from the other ones and cannot be collapsed by translation (in log scale) onto the universal curve, $F(x)$. This might be the origin of the claim

in Ref. [29] that a different scaling is observed at $E = 0$. This is however only a finite-size effect.

In Fig. 14, we show the variations of the localization length ξ as a function of the energy E for different disorder strengths W . In the linear dispersion regime (but not too close to $E = 0$), ξ appears to be a constant whose magnitude increases as W decreases. When getting closer to $E = 0$, ξ decreases (see curve at $W = 2.5J$) and a small dip occurs. A similar feature is predicted in Ref. [30] when computing ξ from the numerically-evaluated semi-classical conductivity. Extrapolating our results, we find that ξ is finite at $E = 0$ but increases sharply when W decreases. Taking graphene as an example ($a = 0.142\text{nm}$, $J \approx 2.7\text{eV}$), the localization length ξ is of the order of $10^6 a \approx 0.1\text{mm}$ at $W = 1.6J \approx 4.32\text{eV}$. This sample size is achievable with the current state-of-the-art technology.

A second notable feature is the small dip slightly below the van Hove singularity at $E = J$. This is surprising as the DoS at the van Hove singularity diverges in the absence of disorder, which implies more propagation channels. Finally we see that ξ decreases as E gets closer

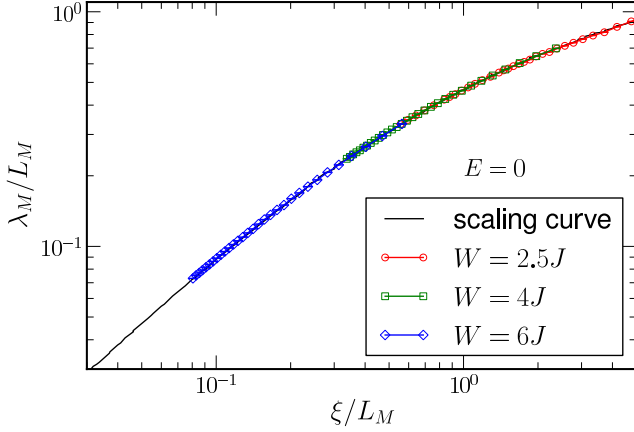


FIG. 12. (Color online) Collapsing AC data obtained at $E = 0$ and disorder strengths $W \geq 2.5J$ onto the scaling function $F(x)$ shown in Fig. 11. For $W = 2.5J$ (circles), $4J$ (squares) and $6J$ (diamonds), we have $\xi = 500a$, $70.9a$ and $16.9a$ respectively. The largest transverse sizes are given by $M = 300$, 70 , and 70 for $W = 2.5J$, $4J$ and $6J$ respectively. Data for $W = 2.5J$ display a small oscillation around the universal curve.

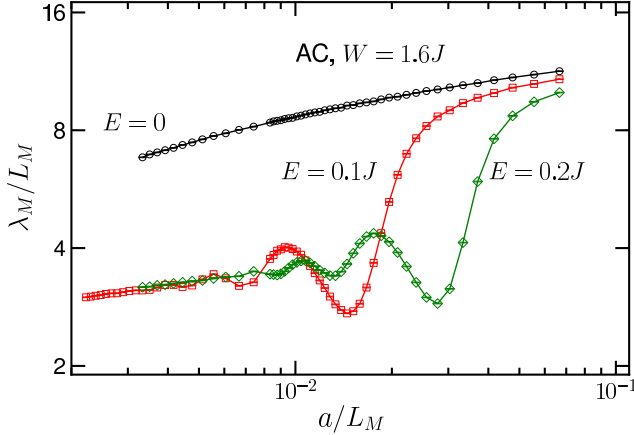


FIG. 13. (Color online) Plot of λ_M/L_M as a function of a/L_M at weak disorder $W = 1.6J$. The oscillations observed at small L_M results from the opening of new scattering channels when L_M is gradually increased. In the linear dispersion regime, the oscillation period in L_M is crudely approximated as inversely proportional to E , with a small correction due to disorder.

to the band edge ($E = 3J$) and slightly extends beyond it.

To conclude this subsection, we compare in Fig. 14 our numerical data near $E = 0$ and $E = 3J$ at $W = 1.4J$ with the analytical prediction of the self-consistent theory of localization [12] (see section VB3). As can be seen, if the general trend is qualitatively satisfactory and even semi-quantitatively correct (within a factor 10) near the band edge, the prediction is off by more than 3 orders of magnitude near the band centre $E = 0$.

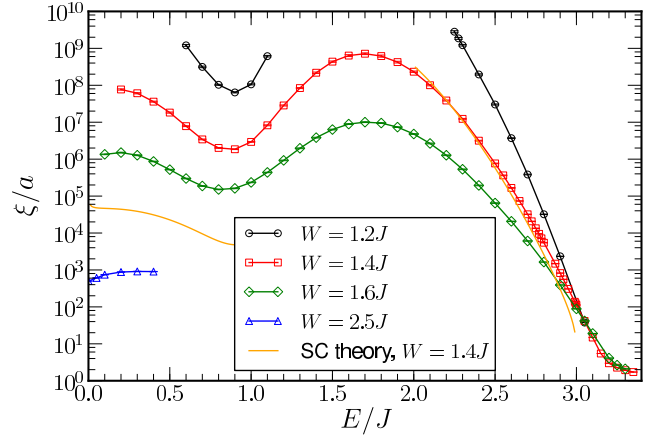


FIG. 14. (Color online) Infinite-lattice localization length ξ (in units of a) versus energy E (in units of J) for various disorder strengths W . For each set (E, W) , ξ is extracted from our numerically-computed λ_M , Eq. (35), with the help of the scaling function $F(x)$ shown in Fig. 11. The orange solid line gives $\xi = 2\ell\sqrt{e^{\pi\kappa\ell} - 1}$ at $W = 1.4J$ as inferred from the self-consistent theory of localization, see Eqs. (45). In this analytical prediction, the scattering mean free path ℓ is estimated using SCBA and κ is defined in Eq. (45). If the qualitative behavior is relatively satisfactory, the quantitative predictions are off by several orders of magnitude in the linear dispersion regime and by about an order of magnitude in the quadratic dispersion regime.

B. Scattering mean free path ℓ

1. RGF numerical estimate

The elastic scattering mean free path ℓ defines the distance a particle travels on average without being scattered. For the negative energy sector (see the reason why in the following subsection), we compute the 1D averaged retarded wave function as

$$\bar{\Psi}_N = \frac{J}{M} \sum_{m,m'=1}^M \overline{\left[G_{n,n+N}^{(N+2n)} \right]_{m,m'}}, \quad (38)$$

where the retarded submatrix $G_{n,n+N}^{(N+2n)}$ connecting slices n and $(n+N)$ is evaluated at complex energy $E + i\eta$ ($E \leq 0$) and disorder strength W , η being a small positive number. The indices m and m' label the sites within each slice respectively. In the following, n is chosen such that the distance between slice n and the closest open-end boundary is large enough (see below).

As shown in Fig. 15, $|\bar{\Psi}_N|^2$ falls off exponentially with a decay constant $\ell(\eta)$. The scattering mean free path is further obtained as $\ell = \lim_{\eta \rightarrow 0} \ell(\eta)$. In our simulations, the number of disorder configurations has been chosen such that we have 2×10^5 samples near the band edge at $-3J$ (quadratic dispersion regime) and 2×10^6 samples near the band centre (linear dispersion regime). We

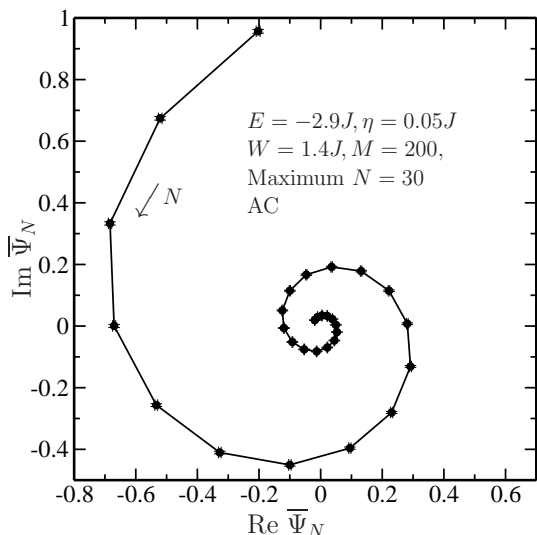


FIG. 15. Disorder-averaged wave function $\bar{\psi}_N$ shown in the complex plane as the longitudinal size of the lattice, fixed by the number of slices N , increases (see arrow for the flow). The plot has been made for the honeycomb AC configuration with $M = 200$ sites per slice. The complex energy is $E + i\eta = -2.9J + i0.05J$ and the disorder strength is $W = 1.4J$. The spiraling feature shows that $\bar{\Psi}_N \sim \exp(ik_w(\eta)L_N) \times \exp\left(-\frac{L_N}{2\ell(\eta)}\right)$, from which we can extract the decay constant $\ell(\eta)$. The scattering mean free path is further obtained as $\lim_{\eta \rightarrow 0} \ell(\eta)$.

have imposed a minimum distance of $5\ell(\eta)$ between slice n and its closest open-end boundary, thereby fixing the value of n in Eq. (38). This ensures that the exponential decay is insensitive to the open-end boundaries. Our numerical results are thus equivalent to those that would have been obtained with an infinite tube. We would like to mention here an important technical remark. When summing the submatrix entries in (38), serious numerical cancellation errors occur when E and J have same signs. In our case $J > 0$ and the numerical evaluation is stable only if $E < 0$. The reason behind this numerical instability is the relative sign between the quasi-Bloch sublattice components of $|\mathbf{k}s\rangle$, see Eq. 7.

The decay constant $\ell(\eta)$ is extracted by performing a linear fit on $\ln|\Psi_N|$ as a function of L_N . We see in Fig. 16 that $a/\ell(\eta)$ displays oscillations similar to those observed for ξ when the transverse size (fixed by the number of sites M) increases. Again, the oscillations can be accounted for by the opening of new scattering channels. By further increasing M , the oscillations damp and finally the fluctuations in $a/\ell(\eta)$ reach the level of the error bars themselves. This happens when the width L_M roughly exceeds $10\ell(\eta)$. Beyond this point, the system does not feel anymore the transverse periodic boundary condition and the corresponding $\ell(\eta)$ are reliable estimates of the infinite-lattice case. We show how to extract ℓ from these reliable estimates in Fig. 17. Note that a direct evaluation of ℓ at $\eta = 0$ is in principle possible,

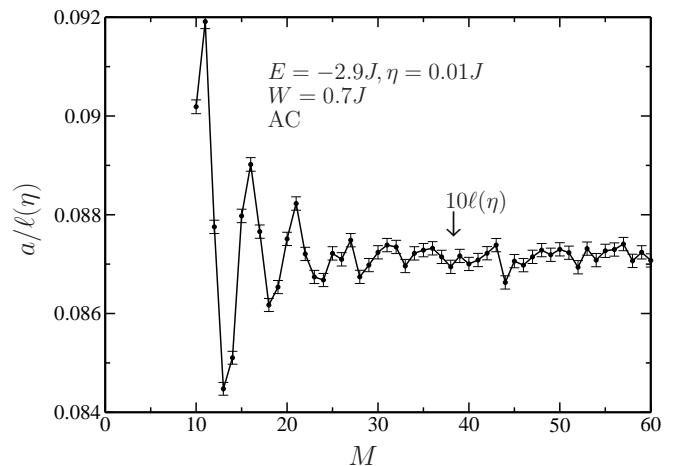


FIG. 16. Oscillation of $1/\ell(\eta)$ as a function of the transverse size M . The oscillation period can be accounted for by the presence of new scattering channels. The oscillation stops when the system does not sense the periodic boundary condition, i.e. $L_M > 10\ell(\eta)$.

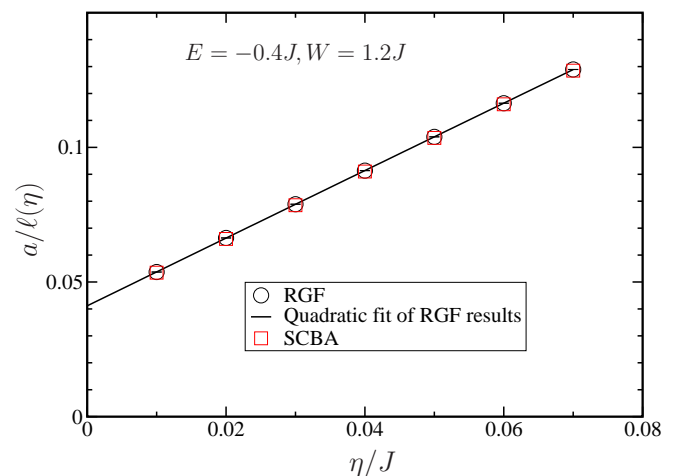


FIG. 17. (Color online) Evaluation of the infinite-lattice scattering mean free path ℓ at a fixed energy E and disorder strength W ($E = -0.4J$ and $W = 1.2J$ in the figure). A sequence of reliable estimates $a/\ell(\eta)$ is first obtained by the RGF technique for smaller and smaller η (black open circles). A quadratic fit (solid black line) is then used to interpolate the value at $\eta = 0$, from which ℓ is deduced. For comparison, we give the results obtained with the SCBA method (open red squares). For the chosen disorder strength the agreement is excellent.

but is unfortunately affected by huge fluctuations as the Green's function is computed on the real axis where its poles lie. This direct method proves thus much less efficient in practice.

2. SCBA estimate

In the same spirit, an SCBA estimate of ℓ can be obtained by using $G_0(E - \Sigma(E))$ in (38) and by considering a finite horizontal lattice strip of length L with periodic boundary conditions in the transverse direction in the limit $L_M, L \rightarrow \infty$. In the limit of an infinite AC honeycomb lattice, a careful but straightforward calculation using Eqs. (7) and (13) leads to

$$\overline{\Psi}_N = J \int_0^{2\pi} \frac{dq}{2\pi} \frac{e^{iNq}}{z + J(1 + 2 \cos q)}, \quad (39)$$

where $z = E - \Sigma(E)$ and $q = \sqrt{3}k_x a/2$. The self-energy $\Sigma(E)$ is computed using Eqs. (22) and (A3). The distance between the two slices being $L_N = \sqrt{3}aN/2$ in the AC configuration, we then get the scattering mean free path as

$$\frac{1}{\ell} = - \lim_{N \rightarrow \infty} \frac{\ln |\overline{\Psi}_N|^2}{L_N}. \quad (40)$$

The exponential decay of $\overline{\Psi}_N$ is given by the imaginary part of the complex pole $Q = Q_r + iQ_i$ solving

$$\cos Q = - \frac{1 + z/J}{2} \quad (41)$$

with $Q_i \geq 0$. The scattering mean free path is then just $a/\ell = 4Q_i/\sqrt{3}$. Approximate solutions are given in the Appendix B.

A word of caution is here necessary. Inspection of (39) in the absence of disorder ($\Sigma = 0$) shows that the allowed energy range is restricted to $-3J \leq E \leq J$. A part of the positive energy sector is thus missed and will keep missed at weak enough disorder. As a consequence using Eq. (39) is only well adapted to the negative energy sector. The physical reason is that the honeycomb lattice has a two-point Bravais cell and the prescription (38) amounts to consider a symmetric combination of amplitudes associated to A-sites and B-sites within a Bravais cell of the initial slice. Would one had chosen the anti-symmetric combination, then one would have gotten

$$\overline{\Psi}_N = J \int_0^{2\pi} \frac{dq}{2\pi} \frac{e^{iNq}}{z - J(1 + 2 \cos q)}, \quad (42)$$

which is well adapted to the positive energy sector. As a rule of thumb, we thus only use Eqs. (38) and (39) for the negative energy sector $E = -|E|$ and then resort to (16) whenever necessary.

Once the scattering mean free path $\ell(E)$ and the scattering mean free time $\tau(E)$ have been calculated, one can compute the ratio $v(E) = \ell(E)/\tau(E)$. From (41), we get

$$\frac{v(E)}{c} = \frac{2}{\sqrt{3}} \sin Q_r \frac{\sinh Q_i}{Q_i}, \quad (43)$$

where c is the Dirac fermions speed and where $0 \leq Q_r \leq 2\pi/3$ for propagation from left to right. At sufficiently

weak disorder, one expects $Q_i \ll 1$, and thus $v(E)/c \approx (2 \sin Q_r)/\sqrt{3}$, where Q_r solves

$$\varepsilon(Q_r) = -J(1 + 2 \cos Q_r) \approx E - \text{Re}\Sigma(E). \quad (44)$$

In the weak disorder regime, the real part of self-energy is generally small compared to the value of E and can be usually discarded.

Returning to fully dimensioned quantities, we thus find the usual result that $v(E) = |\partial_{k_x} \varepsilon(k_x)|/\hbar$ is the group velocity (here along Ox) when disorder is sufficiently weak. Quantitative comparison between the SCBA and RGF results are shown in Figs. 18 and 19. The two methods show remarkable agreement. We note however that the SCBA underestimates ℓ in the quadratic dispersion regime but overestimates ℓ in the linear dispersion regime. The deviation of the Born approximation from the true (RGF) ℓ might be understood from two perspectives: first as a consequence of the smoothing of the DoS $\nu(E)$ by disorder (see Fig. 20), second as a consequence of the enhancement of the group velocity (see Fig. 21 and 22). Indeed, from the relation $\ell = v\tau$ (v is the group velocity), we know that $1/\ell$ is directly proportional to $\text{Im}\Sigma(E)$, which is in turn directly proportional to the DoS. As disorder is increased, the sharp variations of the DoS at the band edges ($E = \pm 3J$), at the van Hove singularities ($E = \pm J$), and at the charge neutrality point ($E = 0$) are smoothed. Since the DoS area must be conserved (particle number is conserved), this smoothing is accompanied by a redistribution of states over energies and by an increase of the DoS at some energies. For example, since the van Hove singularity peaks in the DoS are decreased, there is a corresponding increase of the DoS in the linear dispersion regime. Similarly, as the band edges are smoothed, the DoS at $|E| < 3J$ decreases but increases for $|E| > 3J$. Therefore, the departure of the actual $1/\ell$ from the Born value as disorder is increased, and whether the Born value underestimates or overestimates the actual $1/\ell$ in Fig. 18 and Fig. 19, is a simple consequence of the smoothing effect of the DoS in different energy regimes.

3. Comparison with the self-consistent theory of localization

The self-consistent theory of localization (SCTL) [12] provides a self-consistent recipe which extends the weak-disorder diagrammatic approach to the regime of Anderson localization. The diagrammatic approach describes perturbatively the weak localization corrections to classical transport due to interference along closed loops. As this correction diverges for infinite system size, the self-consistent theory of localization aims at computing the minimum size of the system beyond which the correction is strong enough to stop the diffusive transport and identifies this length scale with the localization length.

For isotropic scattering and an isotropic dispersion relation, SCTL establishes a simple link between the localization length ξ , the scattering mean free path ℓ and the

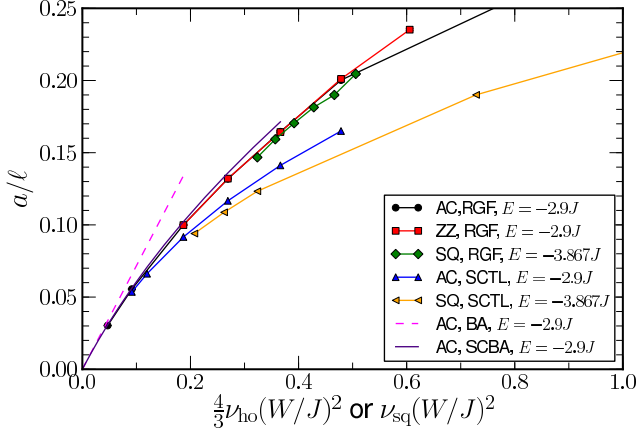


FIG. 18. (Color online) Inverse of the scattering mean free path ℓ (in units of the inverse of lattice constant a) extracted from the recursive Green's function (RGF) method and from the self-consistent Born approximation (SCBA) as a function of the square of the disorder strength W in units of the hopping energy J . To compare results obtained for the honeycomb and square lattices, $(W/J)^2$ is renormalized by a factor proportional to the corresponding densities of states, $\nu_{\text{ho}} = 0.14$ (honeycomb) and $\nu_{\text{sq}} = 0.081$ (square), in the absence of disorder as defined by Eq. (47). For both lattices, the (negative) energy E is chosen near the band edge where the dispersion is quadratic. The inset identifies the different lattices, configurations, energies and calculation methods. The overlap between the results of the armchair (AC) honeycomb and square (SQ) lattices show that the average propagation near the band edge is independent of the lattice type and solely determined by the quadratic nature of the dispersion relation. Comparison with the Born approximation is shown. We also plot the scattering mean free path corresponding to the numerically observed localization length (calculated with the Recursive Green Function method), assuming that the two quantities are connected by eq. (45) derived from the Self-Consistent Theory of Localization. This shows that the predictions of the Self-Consistent Theory of Localization are qualitatively correct, especially for weak disorder, but that large quantitative deviations are observed at large disorder.

wavevector κ ,

$$\xi = 2\ell \sqrt{e^{\pi\kappa\ell} - 1} \approx 2\ell e^{\frac{\pi}{2}\kappa\ell}, \quad (45)$$

where $\kappa = |\mathbf{k}|$ when the energy is chosen near the band edges and $\kappa = |\mathbf{q}| = |\mathbf{k} - \mathbf{K}|$ when the energy is chosen near the charge neutrality point. SCTL being valid when $\kappa\ell \gg 1$, we further get the approximation

$$\frac{\pi\kappa\ell}{2} \approx \ln(\pi\kappa\xi/4) - \ln(\ln(\pi\kappa\xi/4)). \quad (46)$$

We show this SCTL prediction in Fig. 18 and Fig. 19, ξ being evaluated by the RGF method. Much to our surprise, the agreement between our numerical data and the SCTL prediction proves very poor. It should be reminded however that SCTL is supposed to be valid when $\kappa\ell \gg 1$, that is in the weak disorder limit where a/ℓ is

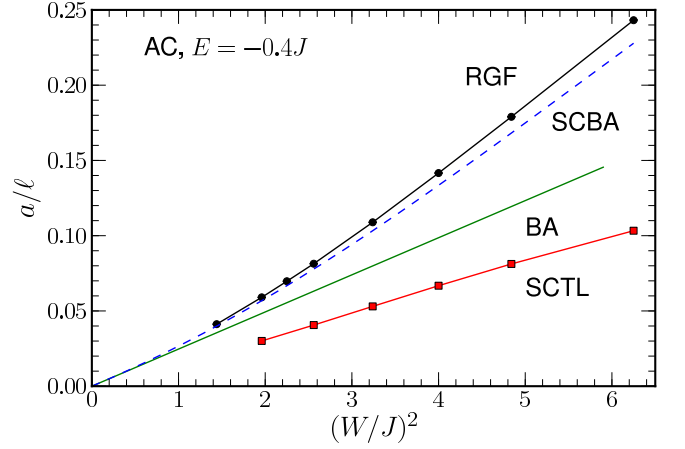


FIG. 19. (Color online) Inverse of the scattering mean free path ℓ (in unit of the inverse of the lattice constant a) as a function of the square of the disorder strength W in units of the hopping energy J for the AC honeycomb lattice. The (negative) energy $E = -0.4J$ is chosen in the linear dispersion regime. Connected filled black circles: RGF results. Blue dashed line: SCBA results. Black solid line: Born approximation (BA). Connected filled red squares: scattering mean free path estimated from the localization length, assuming that they are connected by eq. (45) derived from the Self-Consistent Theory of Localization. While the SCBA prediction agrees well with the RGF numerical computation of the mean free path, the predictions of the Self-Consistent Theory of Localization are quantitatively off.

simply proportional to W^2 . Fig. 18 (and to a lesser extent Fig. 19 too) indeed shows that the SCTL estimate tends to be a linear function of W^2 . In fact all predictions, SCBA, RGF, SCTL and Born approximation agree well when $W \ll J$. It would be desirable to have numerical results at smaller disorder strengths. Unfortunately, the localization length is too large to be measurable. In any case, our numerical results show that higher orders in W are completely different for the true (RGF) a/ℓ and the SCTL prediction. Furthermore, the trend in the linear dispersion regime is completely different. These results are yet to be understood.

C. Density of states

The disorder-averaged DoS per lattice site is defined by

$$\nu(E/J, W/J) = \frac{1}{2N_c} \sum_{\mu} \overline{\delta(E/J - \lambda_{\mu}/J)}, \quad (47)$$

where N_c is the total number of Bravais cells and where λ_{μ} is the eigenvalue of the Hamilton operator H in Eq. (1). This definition is related to the diagonal elements of the Green's function by

$$\nu(E/J, W/J) = -\frac{J}{\pi} \lim_{\eta \rightarrow 0^+} \text{Im} \langle j | \overline{G}(E + i\eta) | j \rangle, \quad (48)$$

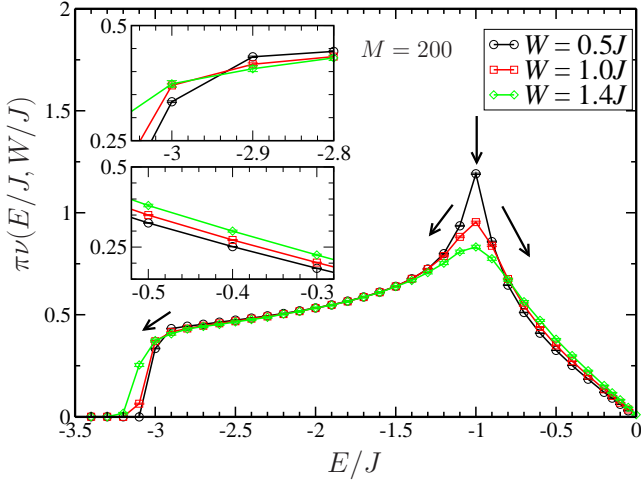


FIG. 20. (Color online) Density of states (DoS) $\nu(E/J, W/J)$, Eq. (48) as a function of (negative) energy E (in units of the hopping energy J) for several disorder strengths W . The number of sites in the transverse direction is $M = 200$. The DoS is increasingly smoothed by disorder as W is increased. Because of particle number conservation, the area under the curve is also a conserved quantity and states are simply redistributed over a broader energy range. For example, as the smoothed van Hove singularity peak at $E = -J$ decreases, the corresponding states are redistributed in the wings as indicated by the arrows. This translates into an increased DoS near the charge neutrality point $E = 0$. Similarly, states at the band edge at $E = -3J$ are partly redistributed outside the energy band of the clean system ($E < -3J$), resulting in a decrease of the DoS in the quadratic dispersion regime $E \gtrsim -3J$. The upper inset shows the variations of the DoS in the quadratic dispersion regime while the lower inset shows the variations of the DoS in the linear dispersion regime near the charge neutrality point.

where j labels an arbitrary lattice site in the infinitely-large lattice. Like what we did to extract ℓ with the RGF method, we compute $\overline{G}(E + i\eta)$ for $\eta/J \in [0.01, 0.07]$ and then perform a quadratic fit in η to extract the limit $\eta \rightarrow 0^+$. For each value of η , the longitudinal length L_N and the transverse width L_M are both chosen to be greater than $10\ell(\eta)$. The value of $\langle j|\overline{G}(E + i\eta)|j \rangle$ is then estimated by considering any site j at a minimum distance of $5\ell(\eta)$ from the two ends of the tube.

The comparison between the DoS calculated with the RGF and SCBA methods is shown in Fig. 23. The two methods agree remarkably well except near the band edges ($E = \pm 3J$) and at the charge neutrality point ($E = 0$). The breakdown of SCBA is probably due to the fact that $q\ell \ll 1$. For moderate disorder strength ($W = 1.4J$), the RGF results display Lifshitz tails near the band edges while the SCBA results show a square-root cut-off.

The DoS at $E = 0$ as a function of W is shown in Fig. 24. The large deviation between the RGF and SCBA results is expected since the latter is strictly not valid in the range of disorder strengths shown. Note that Shon

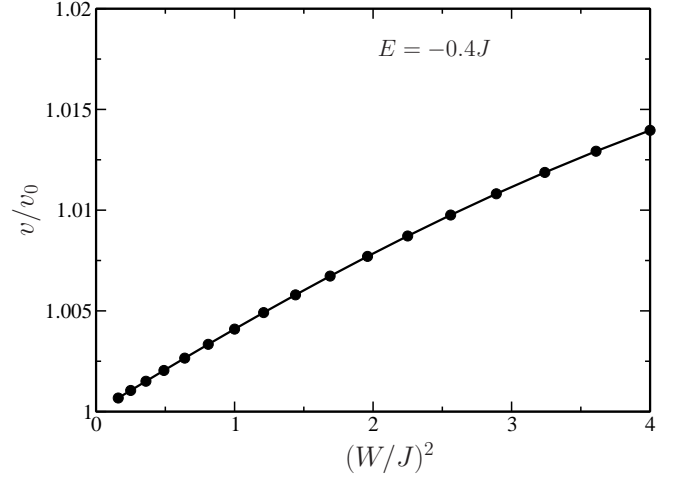


FIG. 21. Variation of the group velocity $v = \ell/\tau$ with respect to the square of the disorder strength W in units of the hopping energy J within the SCBA. The (negative) energy $E = -0.4J$ is chosen near the linear dispersion regime. The group velocity of the clean system (chosen along Ox) is $v_0 = 1.1c$, where c is the massless Dirac particles velocity. As one can see, the group velocity near the charge neutrality point is only slightly enhanced by disorder. The reason why SCBA overestimates ℓ near the charge neutrality point compared to the RGF calculation is thus essentially a consequence of the smoothing of the density of states by disorder, see Fig. 20.

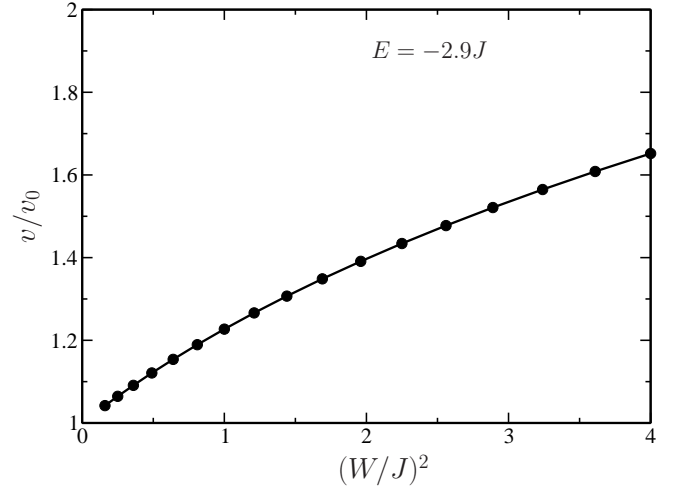


FIG. 22. Variation of the group velocity $v = \ell/\tau$ with respect to the square of the disorder strength W in units of the hopping energy J within the SCBA. The (negative) energy $E = -2.9J$ is chosen in the quadratic dispersion regime. The group velocity of the clean system (chosen along Ox) is given by $v_0 = 0.36c$, where c is the massless Dirac particles velocity. As one can see, the group velocity near the band edge is significantly enhanced by disorder. This is the main reason why SCBA underestimates ℓ near the band edge compared to the RGF calculation.

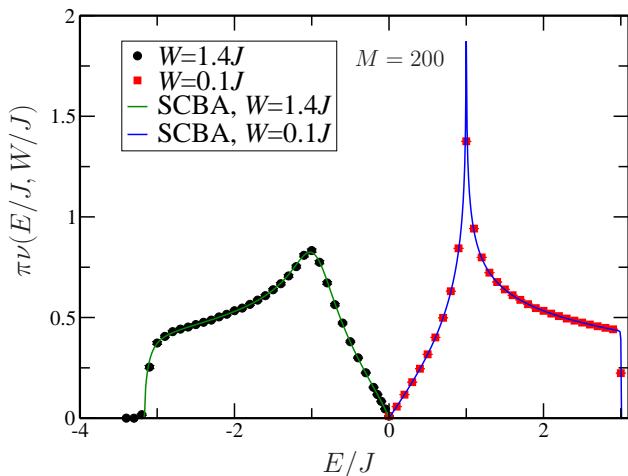


FIG. 23. (Color online) Density of states $\nu(E/J, W/J)$ computed by the recursive Green's function method and by the self-consistent Born approximation at two weak disorder strengths W . The number of sites in the transverse direction is $M = 200$. Since $\nu(E/J, W/J)$ is an even function of E , we have plotted the RGF (symbols) and SCBA (continuous line) predictions at $W = 1.4J$ in the negative energy sector. The corresponding predictions at $W = 0.1J$ have been plotted in the positive energy sector. The agreement is excellent.

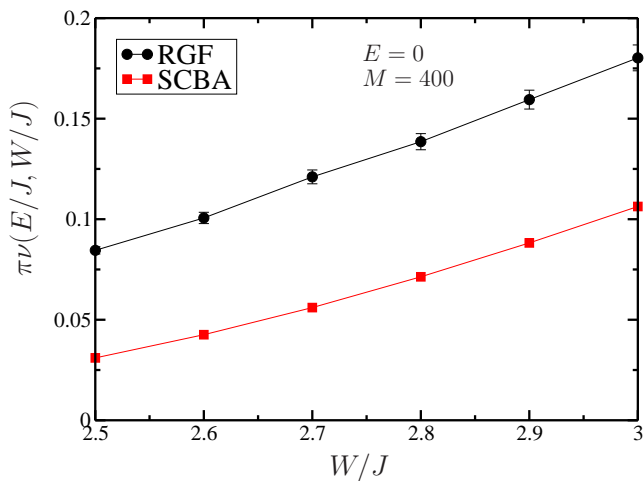


FIG. 24. (Color online) Density of states $\nu(E/J, W/J)$ computed by the recursive Green's function method (full black circles) and by the self-consistent Born approximation (red squares) as a function of the disorder strength W (in units of the hopping energy J) at the charge neutrality point $E = 0$. SCBA underestimates $\nu(E/J, W/J)$ by more than a factor 2 when disorder is large enough. This is the main reason why SCBA overestimates ℓ (see text).

and Ando [35] obtained slightly different SCBA results for the DoS at the Dirac points probably because they used a strictly linear dispersion relation, hence discarding trigonal warping [41]. As already witnessed by the results on ℓ , the SCBA underestimates $\nu(E)$, and hence the self-energy $\Sigma(E)$, in the linear dispersion regime. How-

ever, although quantitatively incorrect, the SCBA qualitatively captures an essential property of the system, namely the very fast decrease of the DoS when W goes to zero, essentially like $\exp(-A/W^2)$.

VI. CONCLUSION

In this paper, we have studied coherent transport in the honeycomb lattice subjected to the effect of a spatially-uncorrelated on-site disorder with symmetric box-like distribution. We have used the recursive Green's function method to reliably extract the scattering mean free path ℓ and the density of states. We have compared these quantities to the analytic predictions of the self-consistent Born approximation and found good agreement at weak disorder. We have also used the recursive Green's function method to extract the localization lengths for different transverse sizes. We have shown that all of these finite-size localization lengths can be collapsed onto a single curve. We have checked that this curve is universal as it applies equally well to the square and honeycomb lattices at any energy. In particular, it applies to the honeycomb lattice at the charge neutrality point, at the van Hove singularities, and at the band edges. These findings validate the one-parameter scaling hypothesis which is thus not restricted to particles with either quadratic dispersion or linear dispersion relations.

ACKNOWLEDGMENTS

LKL acknowledges support from the French Merlion-PhD programme (CNOUS 20074539) and would like to thank M. Schreiber for sharing of data. BG and ChM acknowledge support from the LIA FSQJ and from the France-Singapore Merlion programme (FermiCold grant 2.01.09). The Centre for Quantum Technologies is a Research Centre of Excellence funded by the Ministry of Education and the National Research Foundation of Singapore. ChM is a Fellow at the Institute of Advanced Studies (NTU, Singapore).

Appendix A: Diagonal elements of the clean lattice Green's function

The diagonal elements of the disorder-free lattice Green's function G_0 turn out to be independent of the site i

$$I(z) = \langle i|G_0(z)|i \rangle = \int_{\mathcal{B}} \frac{d\mathbf{k}}{\Omega} \frac{z}{z^2 - J^2|f(\mathbf{k})|^2}, \quad (\text{A1})$$

with $\Omega = 8\pi^2/(3\sqrt{3}a^2)$ the area of the Brillouin zone. We use the rescaling $\sqrt{3}k_x a/2 \rightarrow \alpha$ and $3k_y a/2 \rightarrow \beta$. Defining $Z = z/J$ and $I(z) = H(Z)/J$, little algebra

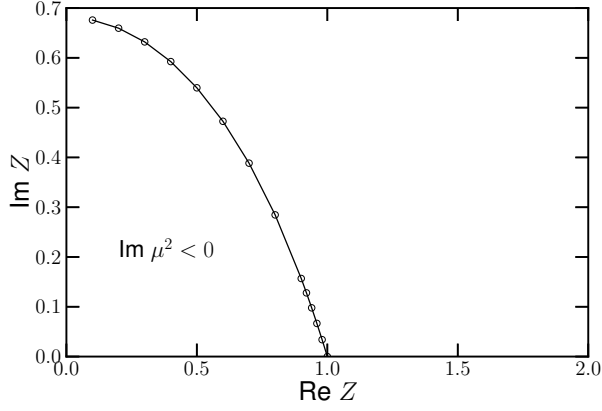


FIG. 25. The boundary $\text{Im}\mu^2 = 0$ (open circles) divides the first quadrant of the complex- Z plane in two regions. The left region satisfies $\text{Re}Z < 1$ and $\text{Im}\mu^2 < 0$. Because of the analytical continuation of the elliptic integral across the boundary $\text{Im}\mu^2 = 0$, different analytic expressions have to be used to compute the rescaled diagonal element of the Green's function $H(Z)$ in these two regions, see Eq. (A3).

gives

$$H(Z) = \iint_0^\pi \frac{d\alpha d\beta}{\pi^2} \frac{Z}{Z^2 - (1 + 4\cos^2\alpha + 4\cos\alpha\cos\beta)}, \quad (\text{A2})$$

where Z can be any point in the complex plane except the real interval $[-3, 3]$.

The idea is now to compute (A2) for real Z outside this interval and do an analytic continuation in the complex plane. In fact, direct inspection shows that $\text{Re}H$ is even in $\text{Re}Z$ and in $\text{Im}Z$, while $\text{Im}H$ is odd in $\text{Re}Z$ and in $\text{Im}Z$. This means that it is sufficient to compute $H(Z)$ in the first quadrant ($\text{Re}Z \geq 0$, $\text{Im}Z \geq 0$) of the complex plane and use these parity properties to infer $H(Z)$ in the other quadrants. By demanding $I(Z)$ to vary smoothly as Z varies in the complex plane and noticing how μ^2 (see below) crosses the branch cut of the elliptic integral, we get [33, 34]

$$H(Z) = \begin{cases} i\Gamma g_0(\Gamma)K(\mu_0^2) & \text{for } Z = i\Gamma, \Gamma > 0 \\ Z g(Z) \left(K(\mu^2) + 2iK(1 - \mu^2) \right) & \text{for } \text{Im}\mu^2 \leq 0 \text{ and } 0 < \text{Re}Z \leq 1, \\ Z g(Z)K(\mu^2) & \text{otherwise,} \end{cases} \quad (\text{A3})$$

where

$$g(Z) = \frac{2}{\pi(Z-1)^{\frac{3}{2}}(Z+3)^{\frac{1}{2}}}, \quad (\text{A4a})$$

$$\mu^2 = \frac{16Z}{(Z-1)^3(Z+3)}, \quad (\text{A4b})$$

$$g_0(\Gamma) = \frac{-2}{\pi(\Gamma^2+1)^{\frac{3}{4}}(\Gamma^2+9)^{\frac{1}{4}}}, \quad (\text{A4c})$$

$$\mu_0^2 = \frac{16 - \left(\sqrt{(\Gamma^2+9)(\Gamma^2+1)} - (\Gamma^2+1) \right)^2}{4(\Gamma^2+1)^{\frac{3}{2}}(\Gamma^2+9)^{\frac{1}{2}}} \quad (\text{A4d})$$

and

$$K(\rho^2) = \int_0^{\frac{\pi}{2}} \frac{d\theta}{\sqrt{1 - \rho^2 \sin^2\theta}} \quad (\text{A5})$$

is the complete elliptic integral of the first kind [42]. Figure 25 gives the boundary $\text{Im}\mu^2 = 0$ in the first quadrant of the complex- Z plane.

Appendix B: Self-consistent Born approximation

1. Van Hove singularities

With the parametrization $\Sigma = \gamma J e^{-i\theta}$, one expects $\gamma \ll 1$ in the weak disorder regime. A small-parameter expansion in Eqs. (22) and (A3), gives at lowest order $\theta \approx \pi/2$ and

$$\frac{4}{\gamma} \ln\left(\frac{4}{\gamma}\right) = \frac{64\pi J^2}{W^2} \quad (\text{B1})$$

Thus,

$$\gamma \approx \frac{W^2}{16\pi J^2} \Omega\left(\frac{64\pi J^2}{W^2}\right). \quad (\text{B2})$$

in terms of the Lambert W -function $\Omega(\alpha)$ defined for any complex number α through the identity

$$\alpha = \Omega(\alpha)e^{\Omega(\alpha)}. \quad (\text{B3})$$

At weak disorder, the asymptotic form for $|\alpha| \gg 1$ [43]

$$\Omega(\alpha) = \ln\alpha - \ln\ln\alpha + \mathcal{O}\left(\frac{\ln\ln\alpha}{\ln\alpha}\right) \quad (\text{B4})$$

yields Eq. (27).

The self-energy in fact obeys the more general relation

$$\Sigma_{\text{SCBA}} = \frac{4J}{\rho + iu} \Omega(e^{-i2\pi/3}(\rho + iu)), \quad (\text{B5})$$

where $\rho = (1 - i4\pi/3)$ and $u = 64\pi J^2/W^2$. Assuming $|\rho| \ll u$, we get from the latter equation $\theta = \pi/2 + \delta\theta$ with

$$\delta\theta \approx \frac{\pi}{6\left(\ln\left(\frac{64\pi J^2}{W^2}\right) - \ln\ln\left(\frac{64\pi J^2}{W^2}\right)\right)}. \quad (\text{B6})$$

2. Band edges

We consider the dimensionless “detuning” $\delta = 3 - E/J$ from the band edge at $3J$. We consider $Z = \delta + \Sigma/J \ll 1$ as a small parameter. Similar to what has been done in the previous Section, we find that Z approximately obeys the equation

$$Z = \beta \left(\ln(12/Z) - i\pi \right) + \delta, \quad (\text{B7})$$

where $\beta = \frac{\sqrt{3}W^2}{48\pi J^2}$. Using the Lambert W -function, we find

$$\Sigma \approx \beta J \Omega \left(\frac{-12e^{\delta/\beta}}{\beta} \right) - \delta J. \quad (\text{B8})$$

The large-argument expansion of the Lambert W -function yields

$$\Sigma \approx \beta J \left(\ln\left(\frac{12}{\beta}\right) - i\pi - \ln \left[\ln\left(\frac{12}{\beta}\right) - i\pi + \delta/\beta \right] \right). \quad (\text{B9})$$

3. Scattering mean free path

For $E < 0$, we solve Eq. (41) to obtain the following approximate solutions:

$$\frac{a}{\ell} = \begin{cases} \frac{4}{3} \frac{\gamma(E)}{\sqrt{1 - \frac{2}{3}\text{Re}(Z)}}, & |E| \ll J, \\ \frac{2}{\sqrt{3}} \gamma(E), & E = -J, \\ \frac{2}{\sqrt{3\delta}} \gamma(E), & \delta = 3 + E/J \ll 1. \end{cases} \quad (\text{B10})$$

We note that the factor $\sqrt{1 - \frac{2}{3}\text{Re}(Z)}$ is needed when the energy is sufficiently far from the charge neutrality point (where deviations from the linear dispersion regime come into play) but not too near the van Hove singularity (where a different approximation applies). Indeed the real part of the self-energy is then no longer small

compared to the energy E itself, at least for the disorder strengths considered. This is the case at $E/J = -0.4$.

Appendix C: Derivation of the generalized version of the recursive Green’s function method

Starting with Eq. (30), the Born series for the Green’s function G_N reads

$$G_N = G_{N-1} + G_{N-1}(H_N^{\text{hop}} + H_N^{\text{slice}})G_N, \quad (\text{C1a})$$

$$G_N = G_{N-1} + G_N(H_N^{\text{hop}} + H_N^{\text{slice}})G_{N-1}, \quad (\text{C1b})$$

where $H_N^{\text{hop}} = H_{N-1,N}^{\text{hop}} + H_{N,N-1}^{\text{hop}}$. In Eq. (C1a), the term $G_{N-1}H_N^{\text{slice}}G_N$ vanishes since H_N^{slice} couples only sites within slice N and one immediately gets Eq. (31a) after sandwiching with bras and kets of sites not exceeding the $(N-1)$ th slice. Furthermore, since, by definition, G_{N-1} does not couple to sites in slice N , we immediately recover Eq. (31b) by setting $n = N$ in Eq. (31a). Eq. (31c) can be obtained from Eq. (C1b) through a similar procedure.

To obtain Eq. (31d), we need to go back to the definition of the Green’s function $(E - H_N)G_N = \mathbb{1}$, which implies

$$(E - H_{N-1} - H_N^{\text{hop}} - H_N^{\text{slice}})G_N = \mathbb{1}. \quad (\text{C2})$$

Sandwiching Eq. (C2) with bras and kets of all sites within slice N , we get

$$EG_{N,N}^{(N)} - H_{N,N-1}^{\text{hop}}G_{N-1,N}^{(N)} - H_N^{\text{slice}}G_{N,N}^{(N)} = \mathbb{1}. \quad (\text{C3})$$

As Eq. (31b) yields

$$G_{N-1,N}^{(N)} = G_{N-1,N-1}^{(N-1)}H_{N-1,N}^{\text{hop}}G_{N,N}^{(N)}, \quad (\text{C4})$$

substitution into Eq. (C3) immediately gives Eq. (31d).

-
- [1] P. W. Anderson, Phys. Rev. **109**, 1492 (1958).
 - [2] M. P. V. Albada and A. Lagendijk, Phys. Rev. Lett. **55**, 2692 (1985).
 - [3] Y. Bidet, B. Klappauf, J. C. Bernard, D. Delande, G. Labeyrie, C. Miniatura, D. Wilkowski, and R. Kaiser, Phys. Rev. Lett. **88**, 203902 (2002).
 - [4] H. Hu, A. Strybulevych, J. H. Page, S. E. Skipetrov, and B. A. van Tiggelen, Nat. Phys. **4**, 945 (2008).
 - [5] S. Faez, A. Strybulevych, J. H. Page, A. Lagendijk, and B. A. van Tiggelen, Phys. Rev. Lett. **103**, 155703 (2009).
 - [6] M. Belzons, E. Guazzelli, and O. Parodi, J. Fluid Mech. **186**, 539 (1988).
 - [7] J. Billy, V. Josse, Z. Zuo, A. Bernard, B. Hambrecht, P. Lugan, D. Clément, L. Sanchez-Palencia, P. Bouyer, and A. Aspect, Nature **453**, 891 (2008).
 - [8] J. Chabé, G. Lemarié, B. Grémaud, D. Delande, P. Szriftgiser, and J. C. Garreau, Phys. Rev. Lett. **101**, 255702 (2008).
 - [9] Z. Cheng and S.-W. Gu, Phys. Rev. B **41**, 3128 (1990).
 - [10] S. Ilani, J. Martin, E. Tetelbaum, J. Smet, V. Umansky, D. Mahalu, and A. Yacoby, Nature **427**, 328 (2004).
 - [11] E. Abrahams, P. W. Anderson, D. C. Licciardello, and T. V. Ramakrishnan, Phys. Rev. Lett. **42**, 673 (1979).
 - [12] D. Vollhardt and P. Wölfle, Phys. Rev. B **22**, 4666 (1980); P. Wölfle and D. Vollhardt, Int. J. Mod. Phys. B **24**, 1526 (2010).
 - [13] R. C. Kuhn, O. Sigwarth, C. Miniatura, D. Delande, and C. A. Müller, New J. Phys. **9**, 161 (2007).
 - [14] P. M. Ostrovsky, I. V. Gornyi, and A. D. Mirlin, Phys. Rev. B **74**, 235443 (2006).
 - [15] A. D. Mirlin, F. Evers, I. V. Gornyi, and P. M. Ostro-

- vsky, *Int. J. Mod. Phys. B* **24**, 1577 (2010).
- [16] K. S. Novoselov, A. K. Geim, S. V. Morozov, D. Jiang, Y. Zhang, S. V. Dubonos, I. V. Grigorieva, and A. A. Firsov, *Science* **306**, 666 (2004).
- [17] Y. Zhang, Y. Tan, H. Stormer, and P. Kim, *Nature* **438**, 201 (2005).
- [18] K. S. Novoselov, A. K. Geim, S. V. Morozov, D. Jiang, M. I. Katsnelson, I. V. Grigorieva, S. V. Dubonos, and A. A. Firsov, *Nature* **438**, 197 (2005).
- [19] E. R. Mucciolo and C. H. Lewenkopf, *J. Phys.: Condens. Matter* **22**, 273201 (2010).
- [20] K. L. Lee, B. Grémaud, R. Han, B.-G. Englert, and C. Miniatura, *Phys. Rev. A* **80**, 043411 (2009).
- [21] P. Soltan-Panahi, J. Struck, P. Hauke, A. Bick, W. Plenkers, G. Meineke, C. Becker, P. Windpassinger, M. Lewenstein, and K. Sengstock, *Nat. Phys.* **7**, 434440 (2011).
- [22] L. Tarruell, D. Greif, T. Uehlinger, G. Jotzu, and T. Esslinger, *Nature* **483**, 302305 (2012).
- [23] G. Labeyrie, D. Delande, C. A. Müller, C. Miniatura, and R. Kaiser, *Europhys. Lett.* **61**, 327 (2003); *Phys. Rev. A* **67**, 033814 (2003).
- [24] D. Clément, A. F. Varón, M. Hugbart, J. A. Retter, P. Bouyer, L. Sanchez-Palencia, D. M. Gangardt, G. V. Shlyapnikov, and A. Aspect, *Phys. Rev. Lett.* **95**, 170409 (2005).
- [25] J. E. Lye, L. Fallani, M. Modugno, D. S. Wiersma, C. Fort, and M. Inguscio, *Phys. Rev. Lett.* **95**, 070401 (2005).
- [26] F. Jendrzejewski, A. Bernard, K. Müller, P. Cheinet, V. Josse, M. Piraud, L. Pezzé, L. Sanchez-Palencia, A. Aspect, and P. Bouyer, *Nat. Phys.* **8**, 398403 (2012).
- [27] M. Greiner, O. Mandel, T. Esslinger, T. W. Hänsch, and I. Bloch, *Nature* **415**, 39 (2002).
- [28] M. Schreiber and M. Ottomeier, *J. Phys.: Condens. Matter* **4**, 1959 (1992).
- [29] S.-J. Xiong and Y. Xiong, *Phys. Rev. B* **76**, 214204 (2007).
- [30] A. Lherbier, B. Biel, Y.-M. Niquet, and S. Roche, *Phys. Rev. Lett.* **100**, 036803 (2008).
- [31] R. Kubo, *J. Phys. Soc. Japan* **12**, 570 (1957).
- [32] E. Akkermans and G. Montambaux, *Mesoscopic Physics of Electrons and Photons*, 1st ed. (Cambridge University Press, 2007).
- [33] T. Morita and T. Horiguchi, *J. Math. Phys.* **12**, 981 (1971).
- [34] T. Horiguchi, *J. Math. Phys.* **13**, 1411 (1972).
- [35] N. H. Shon and T. Ando, *J. Phys. Soc. Japan* **67**, 2421 (1998).
- [36] A. MacKinnon and B. Kramer, *Z. Phys. B* **53**, 1 (1983).
- [37] G. D. Mahan, *Many Particle Physics*, 3rd ed. (Springer, 2000).
- [38] A. MacKinnon, *Z. Phys. B* **59**, 385 (1985).
- [39] D. Wurtz and B. M. Pohlmann, *J. Phys. C* **21**, 5631 (1988).
- [40] C. A. Müller and D. Delande, in *Les Houches 2009: Ultracold Gases and Quantum Information* (Oxford University Press, 2011) pp. 442–533.
- [41] A. H. Castro Neto, F. Guinea, N. M. R. Peres, K. S. Novoselov, and A. K. Geim, *Rev. Mod. Phys.* **81**, 109 (2009).
- [42] I. S. Gradshteyn and I. M. Ryzhik, *Table of Integrals, Series, and Products*, 7th ed., edited by A. Jeffrey and D. Zwillinger (Academic Press, 2007).
- [43] R. Corless, G. Gonnet, D. Hare, D. Jeffrey, and D. Knuth, *Adv. Comput. Math.* **5**, 329 (1996).